Mechanics of the Hysteretic Large Strain Behavior of Mussel Byssus Threads

by

Brian Greviskes

SUBMITTED TO THE DEPARTMENT OF MECHANICAL ENGINEERING IN PARTIAL FULFILLMENT OF THE REQUIREMENTS FOR THE DEGREE OF

BACHELOR OF SCIENCE IN MECHANICAL ENGINEERING
AT THE
MASSACHUSETTS INSTITUTE OF TECHNOLOGY

JANUARY 2008
[February 2008]

Signature of Author: _____
Department of Mechanical Engineering
January 18, 2008

Certified by: _____
Mary C. Boyce
Kendall Family Professor of Mechanical Engineering
Thesis Supervisor

Accepted by: _____
John H. Lienhard V
Professor of Mechanical Engineering
Chairman, Undergraduate Thesis Committee

Mechanics of the Hysteretic Large Strain Behavior of Mussel Byssal Threads

by

Brian Greviskes

Submitted to the Department of Mechanical Engineering
on January 2, 2008 in partial fulfillment of the
requirements for the Degree of Bachelor of Science in
Mechanical Engineering

ABSTRACT

Many biological materials have been shown to demonstrate remarkable physical properties, outperforming even the most widely-used synthetics. This study investigates mussel byssal threads, the attachment appendage of aquatic mussels, which are here shown to exhibit a remarkable ability to withstand very large resilient yet dissipative stretches ($\lambda > 4$) without failing. These threads were dissected into separate regions: proximal (proximal to the mussel) and distal; the sections were then tested in tension in both monotonic and cyclic tests at varying nominal strain rates. These tests demonstrated that each section displayed different properties, and that the behavior of each section was dependent on that section's microstructure. This microstructure, as demonstrated by Hassenkam et. al. (2004), consists of tiny banana-shaped filament bundles, with molecular folded domain ends. It is demonstrated that as the thread is stretched these bundles straighten and the ends unfold, increasing the tension-free length of the filaments. Further stretching is required to load this new length and to release more of the folded domains. Upon unloading these bundles refold, with the refolding being time dependent i.e. as more time elapses between unloading and reloading more of the domains refold. A model for the stress-strain behavior of the threads, based mainly upon this unfolding, is developed. This model captures both the rate-dependence of the material and the thread behavior in loading, unloading, and reloading for both the distal and proximal thread section.

Thesis Supervisor: Mary C. Boyce
Title: Kendall Family Professor of Mechanical Engineering

Table of Contents

Chapter One: Introduction

In recent years, many materials researchers have taken an interest in biological materials, as several have been found to exhibit remarkable properties. The host organisms, because of the harsh demands placed upon them by nature, have evolved these materials to perform highly specific functions. Most famous amongst these is spider silk, which exhibits a toughness unmatched by synthetic materials – even Kevlar (Gosline et. al., 1999). An equally remarkable (though less studied) material is the byssal thread of aquatic mussels.

These aquatic mussels have long been revered for their remarkable ability to remain adhered to the rocks of their aquatic habitat, even in the face of the large and repetitive forces produced by the pounding surf. They do this with the aid of byssal threads, which attach to coastal rocks. Initially these threads provide an elastic response, which allows the mussel to move freely with the waves. As the threads reach a certain strain level, they yield in a manner that retains resiliency yet is highly dissipative. This energy dissipation, keeps the threads from "snapping" back when the force is removed. Without this property, the mussels would be dashed against the rocks with each valley between wave crests.

1.1 Mussel Anatomy

The anatomy of the mussel is quite simple. A foot, which is used for mussel locomotion, connects to the mussel stem (an organic tissue located at the base of the mussel shell). Protruding from the stem are the byssal threads – protein-rich fibers, which vary in diameter from approximately 0.08mm to 0.2mm. As can be seen in Figure 1.1 these threads protrude outward from the stem in a pseudo-circle. The shortest threads (those located at the center of the circle) are rarely more than half a centimeter in length, while the longest (those located at the outermost diameter of the circle) range upwards of 3 centimeters. At the end of each thread is an adhesive plaque, which binds each thread to the rock surface.

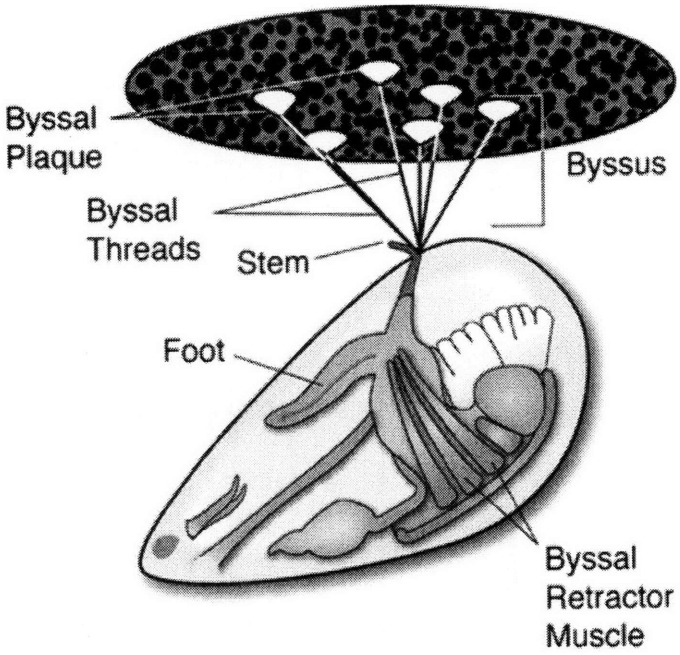

Figure 1.1: Basic anatomy of the aquatic mussel. The threads project out from the stem in a pseudo-circle centered directly beneath the stem (From Silverman and Roberto, 2007).

The protrusions from the stem are random. In some portions of the stem, threads protrude almost on top of each other, while other regions are much more barren. Individual threads also get tangled with their neighbors, giving the perception that the stem/thread interface is a "disordered mess."

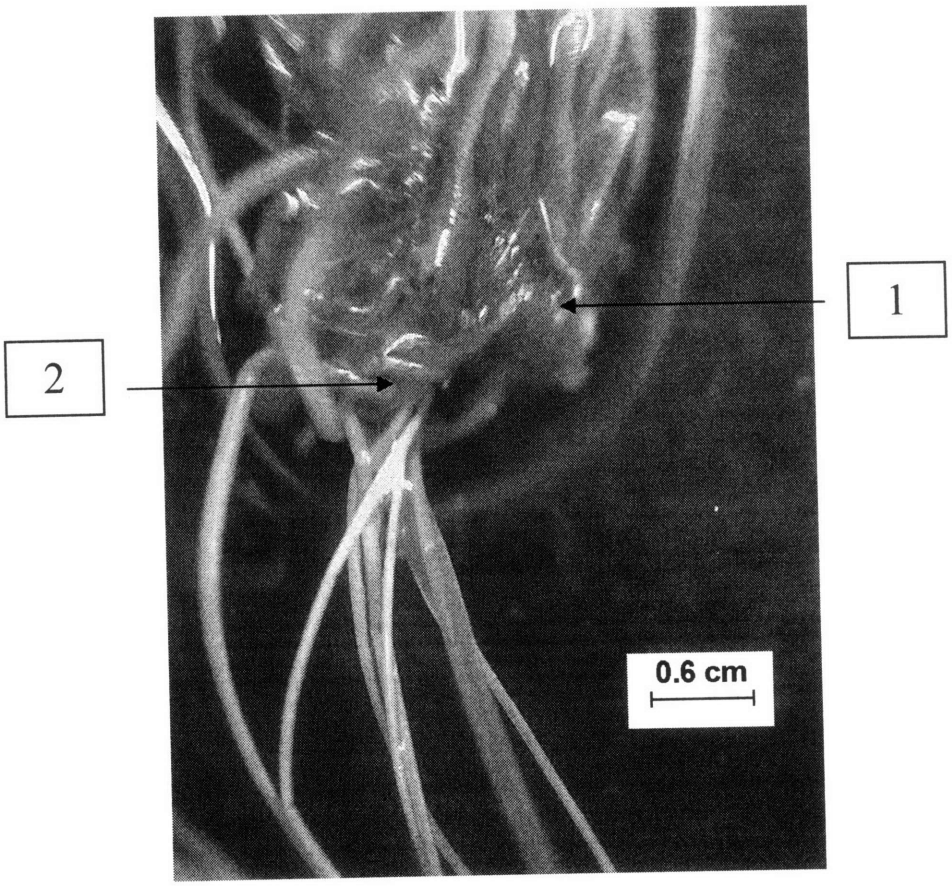

Figure 1.2: Threads protruding from the mussel stem. Region 1 is a thread-barren portion of the stem. Region 2 corresponds to a small grouping of tangled threads. This stem is somewhat atypical in that there is an uncharacteristically large quantity of threads for such a small stem section. However, it does well demonstrate the nature of the thread/stem interface.

However, the pattern of the threads' attachment to the rock surface is not tangled. Rather, individual threads flow outward from the stem, creating a "cloud" of attachments centered beneath the mussels' stem. Thus, whereas the stem is quite small, approximately 3-4mm in length and 1mm in diameter, the attachment cloud can be quite large, forming a pseudo-circle up to 5cm in diameter.

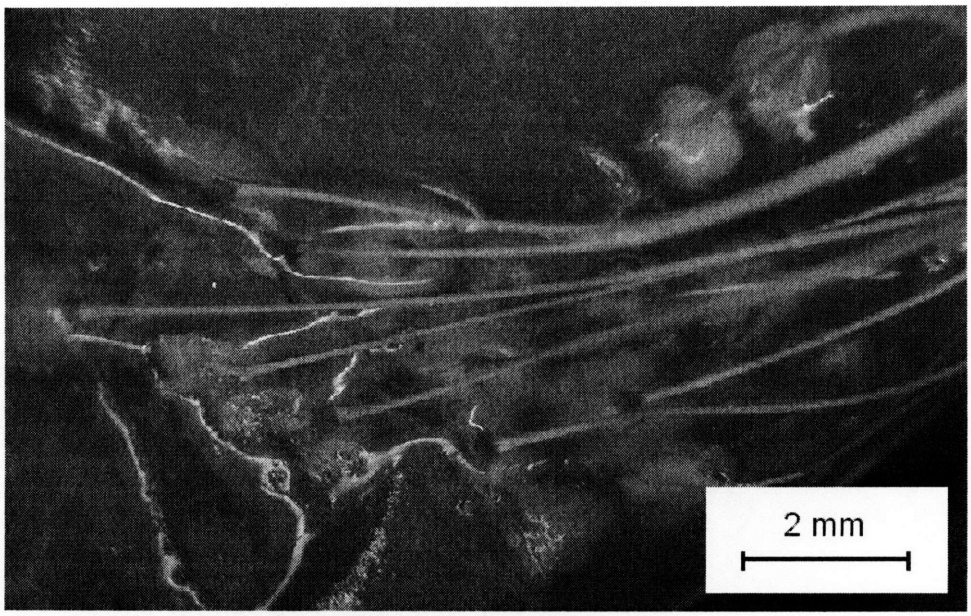

Figure 1.3: Distal ends of byssal threads with adhesive plaques. Adhesive plaques are here attached to a rock surface, with all threads originating from the same mussel. The region shown is only the outermost portion of one edge of the pseudo-circle (this is obvious from the length of the threads). However, this should provide an idea about the great amount of "spreading out" of the threads as they project outward from the stem.

The large dimension of this attachment cloud (as well as the different lengths of the threads) allows for the mussel to resist forces in all directions, so that no matter how the surf pushes or pulls the mussel, there will always be some threads restraining the motion.

1.2 Thread Sections

The thread itself is also ordered, and can be separated into three sections, which differ in microscopic composition, macroscopic appearance, and mechanical properties (Bairati and Zuccarello, 1976; Benedict and Waite, 1986; Bairati 1991; Bell and Gosline, 1996). The three thread sections are the proximal section (proximal to the mussel), the distal section, and the adhesive plaque region at the end of the fiber. Note that the proximal and distal sections are not wholly discrete. Rather, a transitional region exists, joining the proximal and distal regions.

Macroscopically, the thread sections are quite different. The proximal section is much thicker, though also shorter. In most of the threads used here, the length of the proximal region is approximately 25% of the entire thread length (often less than 5mm). It is also more than twice as thick as the distal thread, with the distal thread averaging approximately 0.08mm in diameter and the average proximal thread being 2mm in diameter. The proximal thread is smooth on the surface, while the distal thread has a "crimped-looking" exterior.

Microscopically, the sections are also different. In each section an inner core is surrounded by a jelly-like sheath. This sheath is thin in the distal region – nearly

unnoticeable at approximately 4-5 micrometers – but becomes quite thick in the proximal region, in fact much thicker than the thread core itself (Sun and Waite, 2005).

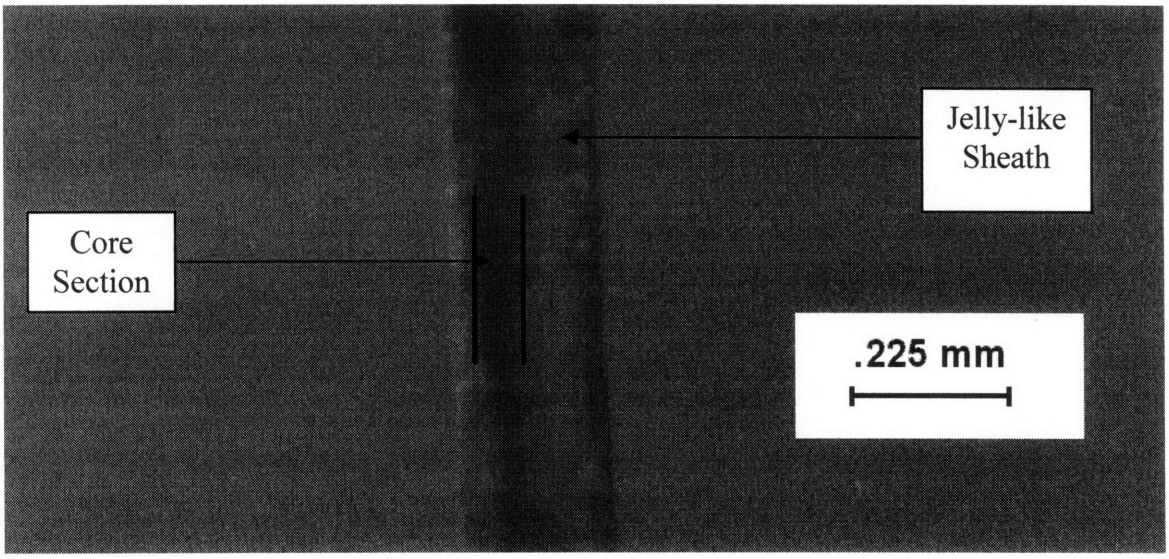

Figure 1.4: Demonstration of jelly sheath in proximal byssal thread. Here the core is seen as the darker section on the far left side of the thread (location is not necessarily center to the thread). The volume occupied by the sheath is much greater than that occupied by the core.

As a final note on thread makeup, it is important to realize that the properties and appearance of the thread sections vary amongst mussel species (Eckroat and Steele, 1993), and that the descriptions given above are consistent with the blue mussel (mytilus edulis) of New England. Other species were not investigated.

1.3 Microstructure

The microstructure of the byssal threads is similar in both the proximal and distal thread regions. A jelly-like matrix surrounds tiny protein-rich filaments. While these filaments are aligned in the distal thread section, pointing along the axis of the thread, they are highly disordered in the proximal region as can be seen in Figure 1.5 (Bairati and Vitellaro-Zuccarello, 1974).

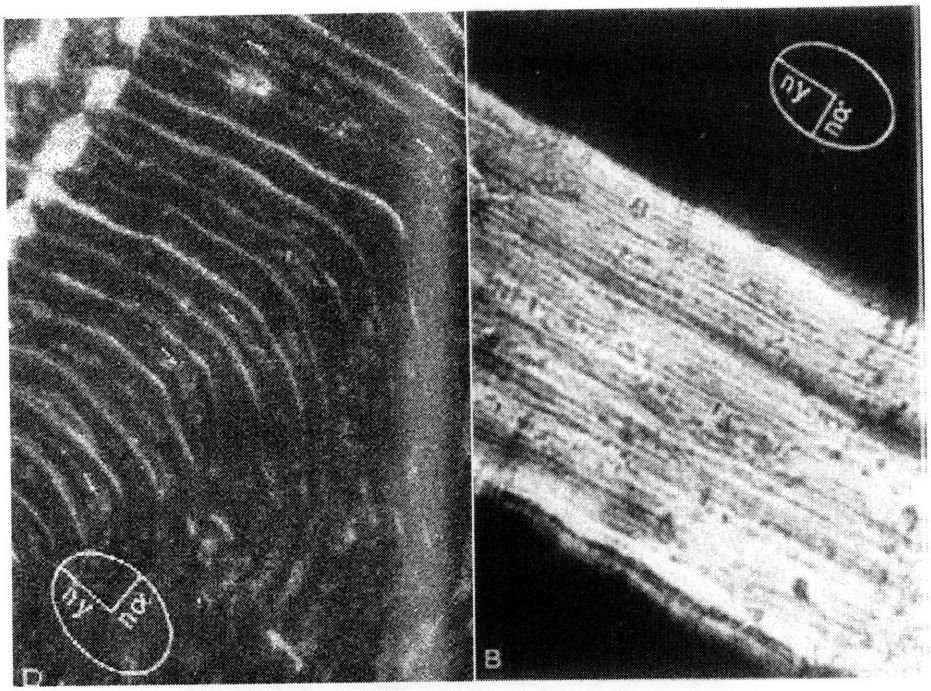

Figure 1.5: Micrographs of proximal cross-section (left) and distal longitudinal (right) thread sections. The streaks in the figure on the right are filaments; these run predominantly in the direction of the thread axis. In the left figure, this streak pattern corresponds to filament spirals, oriented randomly with respect to the thread axis. Both images are magnified X1020 (Bairati and Vitellaro-Zuccarello, 1974).

Because of this, the proximal and distal thread sections must be analyzed separately, with the transitional region also analyzed and used to join the two subsections. Further the sheath, which was discussed above, occupies different volume fractions in the separate thread regions.

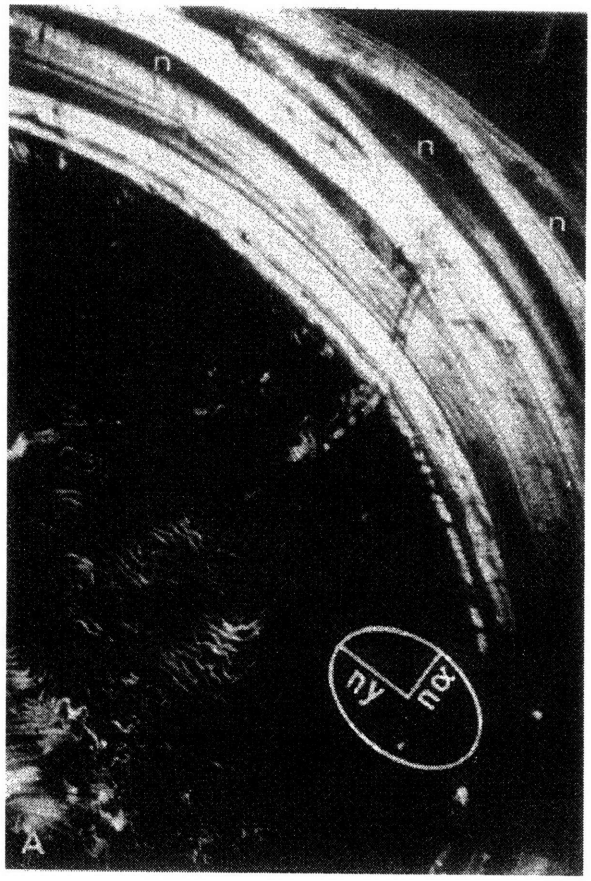

Figure 1.6: Sheath in proximal thread section. The white section corresponds to the sheath and is lighter because it is much less dense than the remainder of the thread (dark).

The microstructure of this sheath is taken to be filament free, since it appears so transparent in contrast to the darker core region (as is evident in Figure 1.6).

The biochemistry of the filaments themselves has been studied in some detail and found to be collagenous (Coyne et al, 1997; Waite et al, 1998). The major component of these filaments is a system of alternating block copolymers (PreCols) alternating between hard blocks and soft blocks. In the distal section, PreCol-D's predominate, while in the proximal section PreCol-P's are most prevalent. These blocks are flanked at either end by elastin-like (in the distal section) or silk-like (in the proximal section) domains and terminate with histidine- and DOPA- sequences. Hassenkam et al. (2004) demonstrate that these filaments are arranged in a banana-shaped bundle, the bundle being a hexagonal 6+1 pattern i.e. a hexagonal arrangement of 6 fibers with 1 fiber in the center (Fig. 1.5). The overall angle of the bundle's bend is 130°, or alternately the deflection from the long axis of the bundle is 50°.

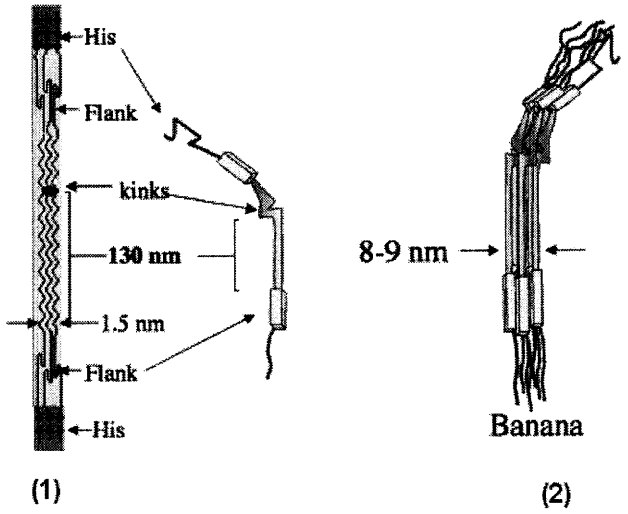

Figure 1.7: (1). Biochemistry of thread filaments. Notice the Histidine and DOPA flanking sequences as well as the much larger internal thread section corresponding to the PreCol's. (2). Banana pattern of the filament bundles (From Hassenkam et. al., 2004).

As can be seen in Figure 1.7 (2) above, these filaments are arranged such that the central regions of the filaments are straight, with the termini of the filaments folded back over each other and held together with secondary chemical bonds. This folded nature of these filament bundles is extremely important, as it has been shown to be a major deformation mechanism in many structural proteins (Alper, 2002).

1.4 Deformation Mechanisms

The major deformation mechanism of these threads has been taken to be the unbending, stretching, and unfolding of these banana-shaped protein bundles. Initially the bundles unbend. When the unbending is complete, the bundles stretch. When a certain threshold force is met, the secondary bonds holding the folded regions together break apart and the folded regions stretch apart.

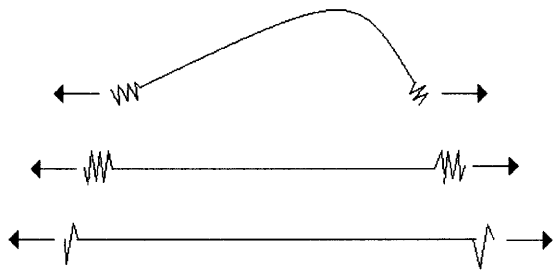

Figure 1.8: Schematic of bundle unfolding. Initially the bundle unbends. Then, the inner core stretches, and finally the folded end domains unfold giving extra length.

Since the bonds are all different (some hydrogen bonds, some ionic, Van der Waals, etc.), the strength of each individual bond is different. Thus, the bonds break at different loads corresponding to different strain levels, with the weakest bonds breaking and releasing additional length that must be tensioned before the stronger bonds can be broken. When all the bonds are broken and the filaments have straightened completely, the fiber reaches some maximum length and the thread fails.

This behavior is captured with the following equation:

$$P = \frac{AE}{L}\delta \tag{1.1}$$

Imposing a deformation increases δ. This consequently increases the load P. When P increases a sufficient amount, it breaks the weakest secondary bonds releasing a distinct increment in additional length (L). The load then suddenly drops, since when L increases at a given δ, A, and E, P must decrease. This process is repeated as the thread is further stretched i.e. the force increases until it reaches the threshold value required to break the next weakest secondary bond. This continues until all the folded domains unfold and stretch. Eventually the entire thread (with all bundles unfolded) will fail. It is important to note that the overall curve increases a small level with stretch, since the unfolding of each subsequent folded domain requires a slightly larger force than the prior domain. The result of this phenomenon is a saw-toothed curve.

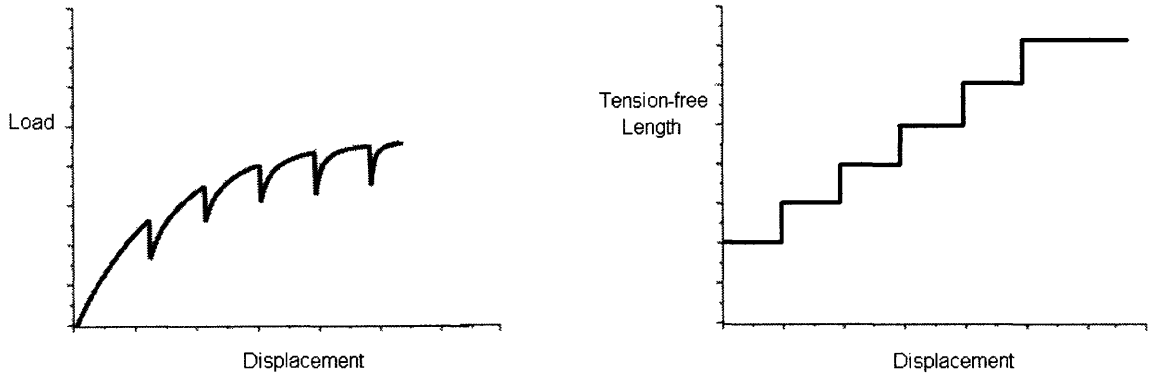

Figure 2.2: Characteristic curves for the loading of a filament bundle. As secondary bonds break, the tension-free length of the bundle instantaneously increases and (per Equation 1.1) the load instantaneously decreases. The overall load increases with displacement, since each secondary bond is stronger than the one broken immediately before.

Individual bundles were not tested in this thesis, but similar filaments from different materials have been tested in the past, and this behavior has been demonstrated (Rief et. al. 1997).

1.5 Experimental and Modeling

In order to investigate the mechanics of these threads, an array of tests, both cyclic and monotonic at several nominal strain rates were run on these threads (proximal and distal separately). In examining the results of these tests, special attention was paid to the microstructure of the separate sections (as discussed above), and this microstructure was used to develop two separate but related models for the stress-strain behavior of the threads. In the chapters that follow, the experimental setup as well as the results of the experiments will be outlined and discussed. The development of the model will also be outlined with all pertinent equations given. Finally, the results of simulations from this model are demonstrated and overlaid with the experimental data to demonstrate the ability of the model to predict the material behavior.

Chapter Two: Experimental Methods

2.1 Experimental Procedure

2.1.1 Specimen Preparation

Mussels were acquired from Georges Island, an island in Boston Harbor (Massachusetts). These mussels were stored in a saltwater tank in our laboratory. Prior to testing, the mussel stems were pulled outward from the shell and a portion of the stem was removed. Threads were then removed from this stem section, with the proximal end being severed with a razor blade immediately adjacent to the stem. The threads were then separated into regions by sight (note that the difference in diameter between the proximal and distal thread regions is noticeable with the naked eye). The distal adhesive plaque was severed from the distal thread, so that it would not interfere with ability to grip the specimens during testing.

Prior to thread removal, thin cardboard specimen holders were prepared. These specimen holders were a necessity, because the small dimensions of the threads made handling them extremely difficult and gripping (in the testing machine) effectually impossible. Further, excessive handling dried out the specimens – leading to dubious experimental results, and using tweezers to position the specimens in the grips caused damage to the threads, rendering them un-testable. These holders contained an open region approximately 3 mm in width and 2mm in height – corresponding to the gauge length of the specimen. The large cardboard tabs on the top and bottom of the holders were used to grip the specimens, while the cardboard strips around the edges of the holders kept the specimens stiff, so that the threads would not break or strain when being placed in the grips (these side strips were cut once the specimen was secured in the grips). Threads were glued between two specimen holders using a quick-drying epoxy. While the adhesive dried, the specimens were kept hydrated with saltwater using an eyedropper. The epoxy hardened enough to allow testing within approximately 30 minutes.

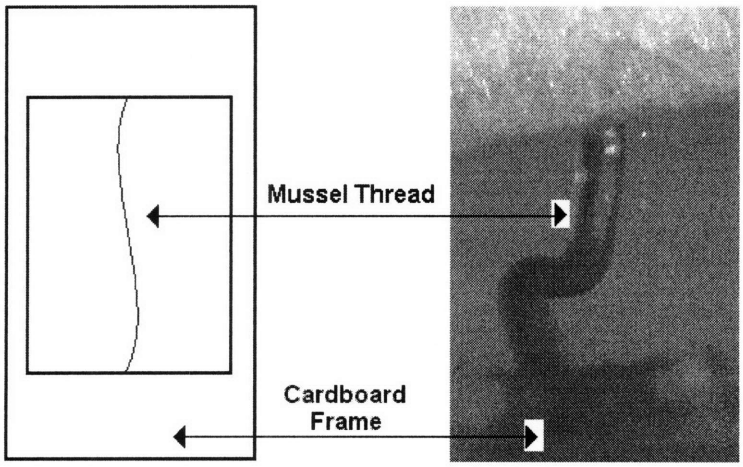

Figure 2.1: Schematic of specimen holders, and actual mussel thread positioned between grips. Amplification of thread image is 10X.

Prior to testing, the diameter of each thread was measured. This was accomplished using the microscope in a Leitz micro-hardness tester. This machine had an objective with a scale, and the thread diameters could be determined from this scale. Most distal threads ranged in diameter from 0.06-0.11mm and most proximal threads ranged in diameter from 0.175-0.25mm.

2.1.2 Experiments

Once the specimens had been prepared and the thread diameters had been measured and recorded, they were secured in the grips of a Bose Enduratec Testing Machine. An array of cyclic and monotonic tests was run on both the proximal and distal thread sections at varying strain rates (note that only one test was run on each specimen). The accompanying load/displacement data was reduced to nominal stress, nominal strain, true stress, and true strain data, with the following equations:

$$\sigma_{nom} = \frac{F}{A_c} \tag{2.1}$$

$$\varepsilon_{nom} = \frac{\Delta L}{L_{initial}} \tag{2.2}$$

$$\sigma_{true} = \frac{F}{A} = \sigma_{nom}(1 + \varepsilon_{nom}) \tag{2.3}$$

$$\varepsilon_{true} = \ln(1 + \varepsilon_{nom}) \tag{2.4}$$

where F is the applied load, A_c is the initial cross-sectional area of the thread, A is the current cross-sectional area, ε is the strain, σ is the stress, $L_{initial}$ is the initial length of the thread, and ΔL is the change in thread length as a result of the applied load. Relations 2.3 and 2.4 (those between true stress-strain and nominal stress-strain) assume an incompressible material (such that $A_c L_{initial} = AL$), which the mussel threads are (or can be approximated as). This data was subsequently used to get a variety of different plots, including plots of stress vs. strain, load vs. deformation, and others. These plots provide the material stress-strain behavior and will also be used to verify the model.

A camera with a microscope lens was utilized during testing to monitor the threads, ensuring that twisted threads and tests in which threads slipped out of the grips could be discounted (these issues were extremely problematic prior to the utilization of imaging equipment). The tests were also videotaped so that each test could be reviewed if the accompanying stress vs. strain curves yielded dubious results. This imaging allowed for the disproval of several outlying curves, which did not follow the norms seen in the majority of tests. Further, imaging proved to be extremely helpful in determining the macroscopic evolution of the threads during testing, especially the evolution of the core and sheath in the proximal thread sections.

An example of the thread extension at different strains is shown here in steps (1) – (4).

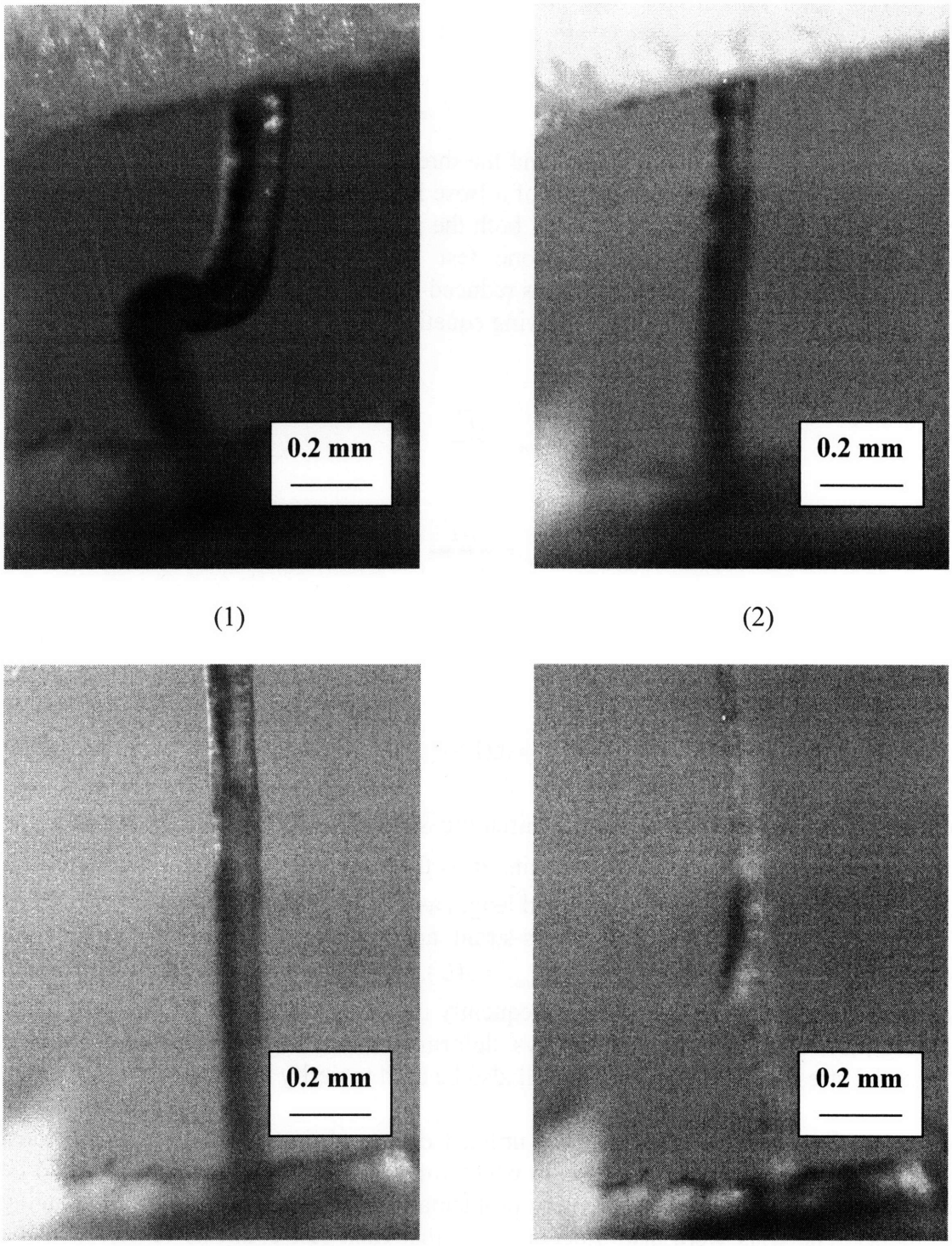

Figure 2.2: Proximal byssal threads at different strains. (1) is at no strain, (2) is at a nominal strain of approximately 0.5, (3) is at a nominal strain of approximately 1.5, and (4) is at a nominal strain of approximately 3.

Although the small nature of the threads made testing difficult, it was the biological nature of the specimens that proved to be most trying. Unlike synthetic materials, biological materials vary and hence yield results that are not very repeatable from one sample to another. Thus, twenty or more specimens were tested for each type of test to ensure that good average value stress/strain data could be acquired. The data is plotted in three different ways below; either the entire set of curves is plotted, a curve that was found to be representative is plotted, or an average curve, with error bars is plotted. Full curve sets for each test are given in the appendix.

2.2 Results and Discussion

2.2.1 Proximal behavior

Monotonic tests to failure, as well as cyclic tests with different hold times between cycles, were run on the proximal thread sections. These tests together demonstrate the initial elastic response of these threads as well as their yield and post yield behavior which, as discussed in the introduction, is believed to result from the unbending, stretching, and subsequent unfolding of the filament bundles. The initial unbending and stretching gives the elastic response; the breaking of the secondary bonds and unfolding of the folded domains gives a yield-like phenomenon. This phenomenon is ongoing with strain, adding compliance to the behavior which becomes evident with unloading and reloading.

The axial load-strain behavior seen in Figure 2.3 is characteristic of a proximal thread section. After the initial elastic response (corresponding to a collective combination of filament bundles unbending and stretching), there is an apparent yielding of the thread at very large strain $(\varepsilon \approx 0.75)$ evidenced by a rollover of the load-nominal strain curve.

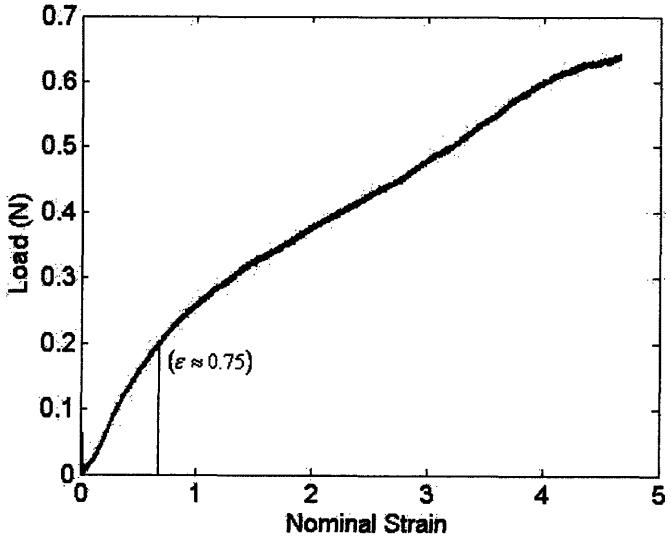

Figure 2.3: Load vs. nominal strain for proximal thread section at a nominal strain rate of 0.1/s.

As can be seen in the load-strain curve for the proximal thread section, the thread shows the initial elastic behavior, with a yield at a load of approximately 0.2N (nominal strain of 0.75). This yield is also evident in a nominal stress vs. nominal strain plot (Figure 2.4).

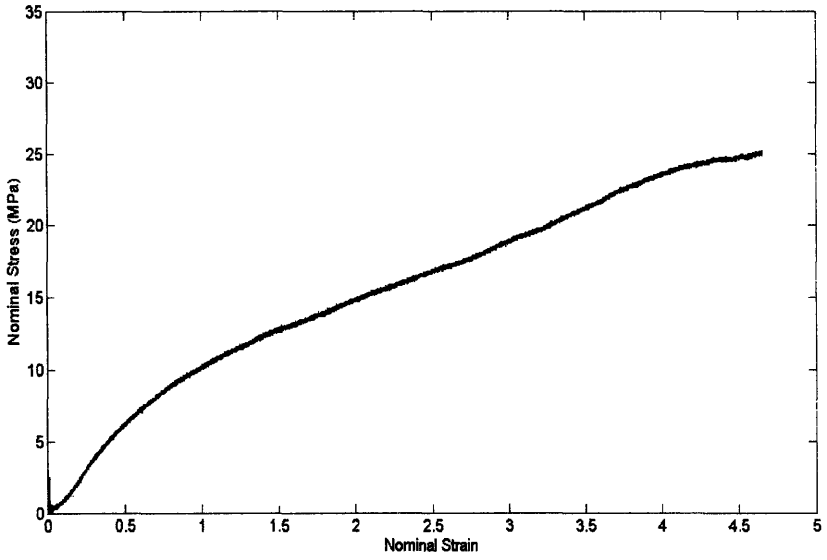

Figure 2.4: Nominal stress vs. nominal strain for proximal byssal threads at a nominal strain rate of 0.1/s.

The curve has the same basic shape (scaled obviously by the initial area of the thread). The yield is quite evident at similar values of nominal strain (nominal stress approximately 7.5MPa). This yield however, is not evident in true stress vs. true strain plots (Figure 2.5).

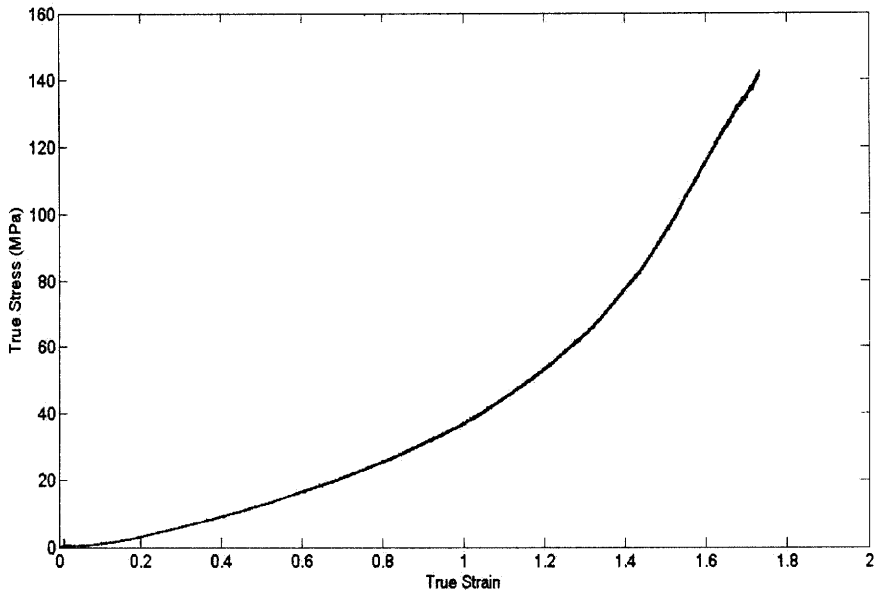

Figure 2.5: True stress vs. true strain for proximal byssal threads at a nominal strain rate of 0.1/s.

This curve appears quite smooth throughout, and no initial yield is evident. The reason for this is that true stress and strain account for the evolution of the cross-section of the specimen, unlike nominal stress and strain which are based only on the initial cross-section.

The implications of this phenomenon (no apparent yield in the true stress-true strain curve) are extremely important, because it demonstrates that this "yield" is not the same yield as in conventional metals or plastics, since it occurs at large strain and is not accompanied by significant plastic deformation. Rather, for the byssal threads, it is hypothesized that the deformation is not a sum of plastic and elastic components (as it is in conventional materials), but rather some function of filament unfolding and refolding.

To test this hypothesis, cyclic tests were performed. If the hypothesis is correct, then either the originally folded regions at the ends of the bundles would refold upon unloading and the reloading curve would match the initial loading curve, or these regions would not refold in which case there will be some residual "plastic" strain and the reloading curve would follow the unloading curve, giving a more compliant behavior than the original.

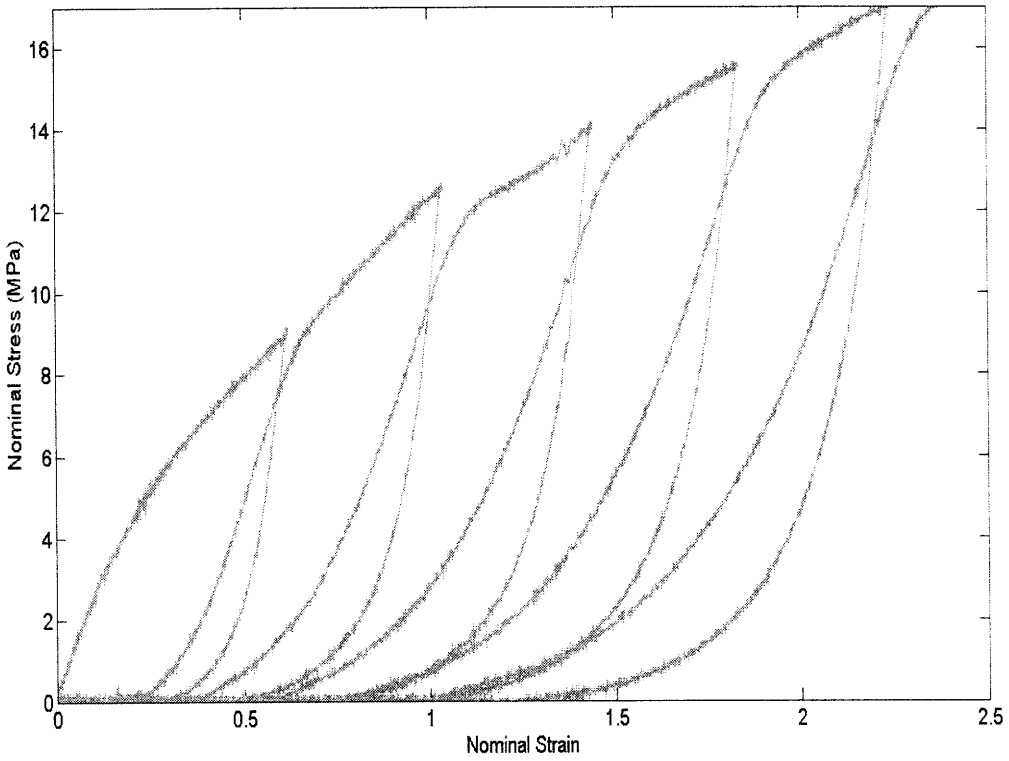

Figure 2.6: Cyclic loading of proximal thread section at a nominal strain rate of 1/s. No hold time was used between cycles i.e. the thread was strained to some displacement value then brought back to zero then strained to a higher strain value right away.

The cyclic loading behavior seen in Figure 2.6 is characteristic of neither condition discussed above. Here the initial loading curve increases as a normal monotonic test. Upon unloading the stress drops off quickly with strain and quickly returns to zero. Upon reloading, the stress remains at zero for some time, until just before it reaches the unloading curve. Then, the stress increases quickly with strain until it reaches the value of stress and strain (approximately) from which it was originally unloaded and the reloading curve then again begins to look like what would be expected in a simple monotonic test. This behavior is the same for subsequent unloadings and reloadings.

From this behavior, it is obvious that the regions did not fully refold, as that would produce a reloading curve similar to the initial loading curve. However, the regions also did not remain completely unfolded, as that would give a curve similar to conventional materials. Thus, some intermediate amount of refolding must have occurred, with some regions refolding, and others remaining unfolded. A look at the true stress-true strain curve for this test provides additional insight.

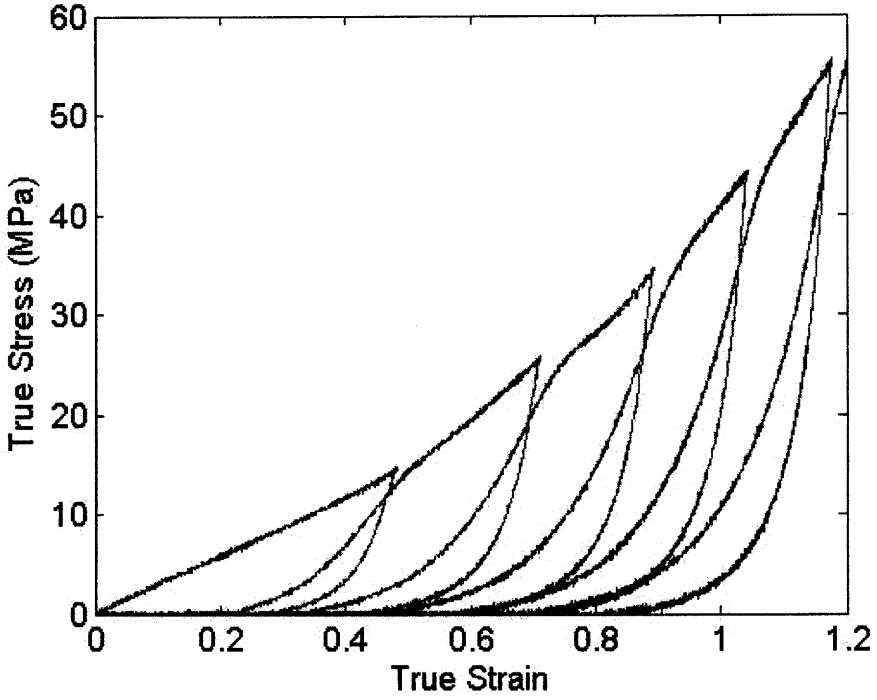

Figure 2.7: True stress vs. true strain for proximal byssal threads in cyclic loading. The test was conducted at a nominal strain rate of 1/s, with no hold time in between cycles.

Here again it is obvious that there is some refolding, but that the threads do not reform into their original conformation instantaneously upon reloading.

A cyclic loading test had been conducted also at a slower strain rate (Figure 2.8) to demonstrate the rate dependence of the proximal thread region, and although it did demonstrate that the material is rate dependent i.e. that for a given strain, the stress is higher in higher rate tests, it also demonstrated that this fractional refolding is rate-dependent.

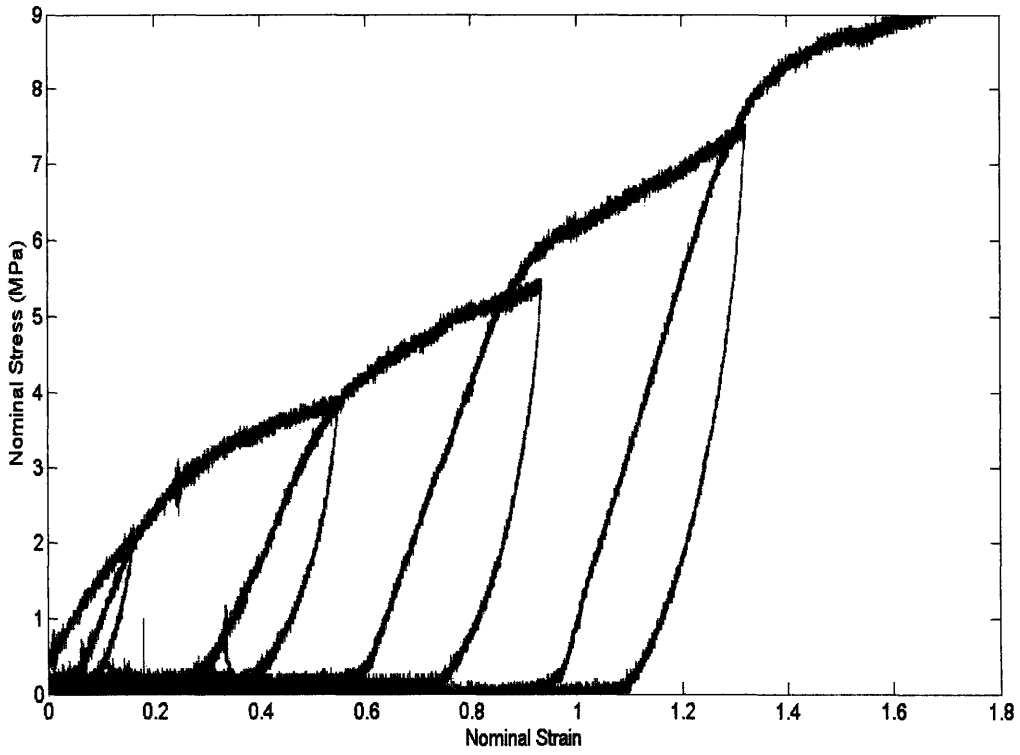

Figure 2.8: Cyclic loading of proximal byssal threads at a nominal strain rate of 0.01/s.

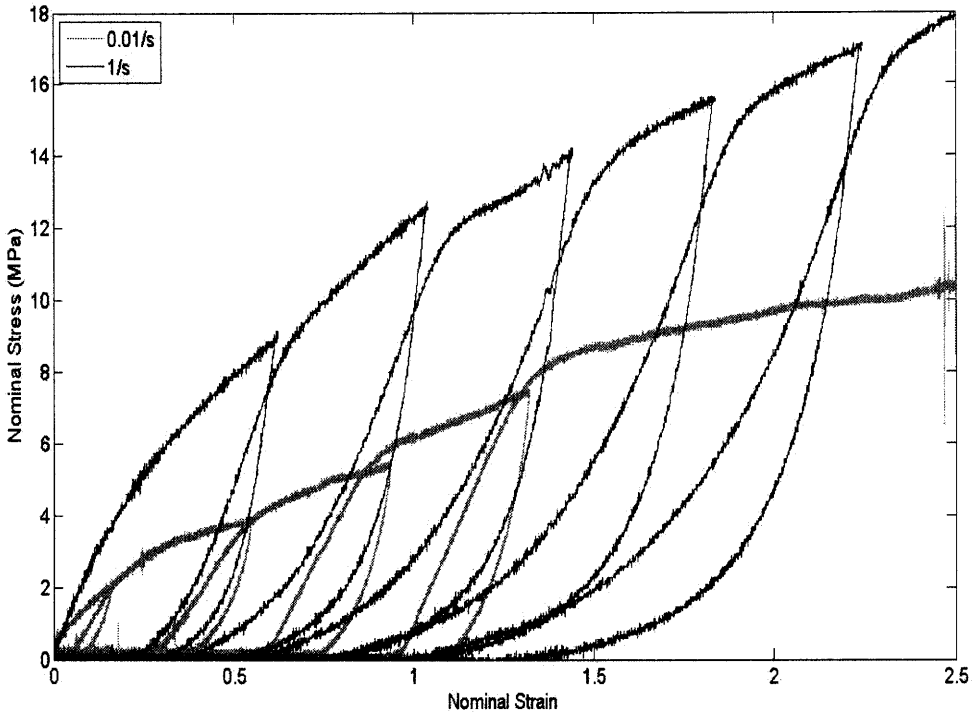

Figure 2.9: Nominal stress vs. nominal strain for cyclic tests of proximal byssal threads at two strain rates (1/s and 0.01/s).

In Figure 2.9 it appears that the reloading curves look to follow the original loading curves more closely than they did in the test at nominal strain rate of 1/s (Figure 2.6), as is evident by the fact that the regions between unloading and reloading are much wider. Thus, the refolding must be rate-dependent i.e. there is some refolding during unloading, and the amount of refolding will increase if the thread is held at no load for a long enough time. In this case, the time held at no load was not different (since again no hold time was used between cycles), but since the rate was so much slower, it inadvertently introduced some time at no load. Thus, another test was run, this time with a true hold time in between cycles to determine the validity of this hypothesis.

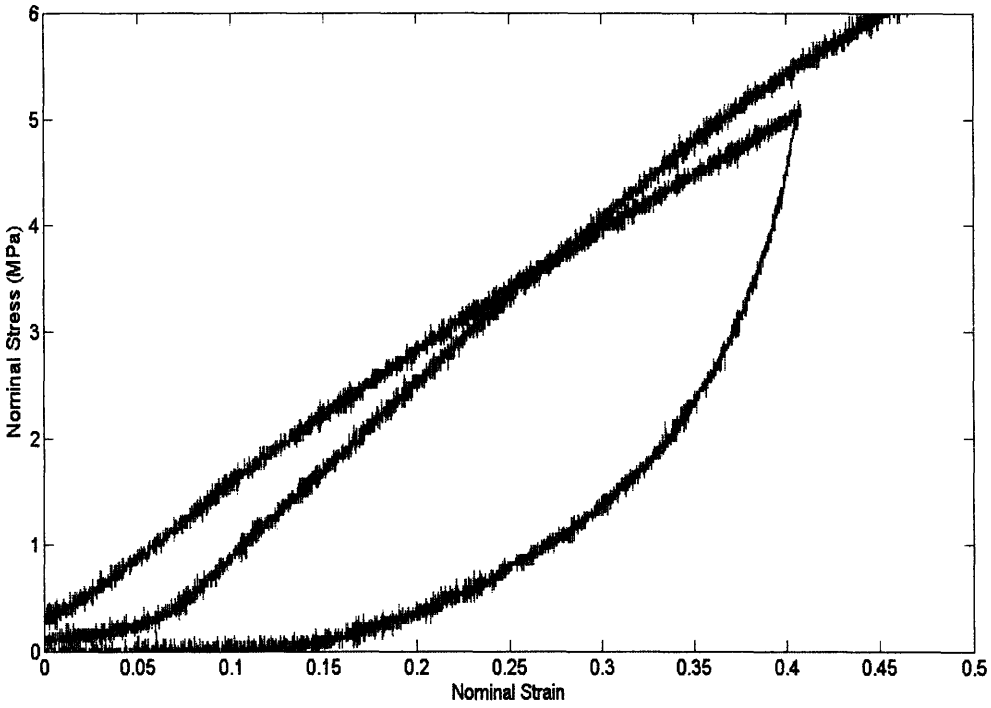

Figure 2.10: Nominal stress vs. nominal strain for proximal thread section in a cyclic tension test. 3 minutes of hold time was used between cycles i.e. the thread was strained to some displacement value then brought back to zero and held for 3 minutes before the thread was again strained. Test was run at a rate of 0.1/s.

Figure 2.10 depicts nominal stress vs. nominal strain for cyclic loading of the proximal thread with a 3 minute hold time between cycles. As can be seen in the figure, the stress-strain curve in reloading is much closer to the initial loading curve (relative to the curves seen in Figure 2.9). This demonstrates that the refolding of the filament ends is indeed time dependent.

There is a combination of thermodynamics and chemical kinetics that govern the refolding phenomenon, but basically the protein looks for the configuration which requires the least energy. This requires that certain amino acid sequences "find each other" forming high strength bonds. This process however requires time, since the odds of the protein unloading such that the "right" amino acids sit next to each other is for all intensive purposes zero. Indeed, 3 minutes is not even enough for this "perfect" refolding, since the two curves do not perfectly align. Tests with longer hold times (though they were not run) should yield curves that align even better than that seen in Figure 2.10. Note that similar results were demonstrated by the Waite group (Sun 2001) for cyclic loading with a hold time, but did not show results for tests without a hold time between cycles.

Finally, it is important to investigate the results of assuming a different diameter for the proximal thread. In the cyclic tests above, the diameter of the thread was taken to be the thread's entire diameter, which (as discussed in the introduction) consists of an inner core and a surrounding jelly-like sheath. Both thread sections, the proximal and distal, have this inner core/jelly-filled sheath structure. However, in the distal section, this sheath is a tiny amount (in volume percentage) of the entire thread. In the proximal thread section, this sheath accounts for the majority of the volume percentage of the thread. Thus, if we consider that the majority of the load is carried by the inner fiber core (a reasonable assumption since the main deformation mechanism is taken to be the stretching and alignment/orientation of the protein filaments), an "effective" diameter, equal in value to the diameter of the inner core, can be used to determine the stress and strain on the fiber.

However, the determination of the diameter of this inner core region is nontrivial. This is because the apparatus used for determining the diameter of threads is not sensitive enough to see variation in filament density across the thread. Thus, no good way of determining the actual diameter of the inner core is possible. So, a simple percentage is here employed. It was observed (in most cases) through simple visual observation that the diameter of the inner core appears to be approximately 20-40% of the fiber. Therefore, its diameter will be taken to be 30% of the diameter of the thread itself. Images for proximal byssal threads at two values of strain are given here (the core is highlighted with arrows):

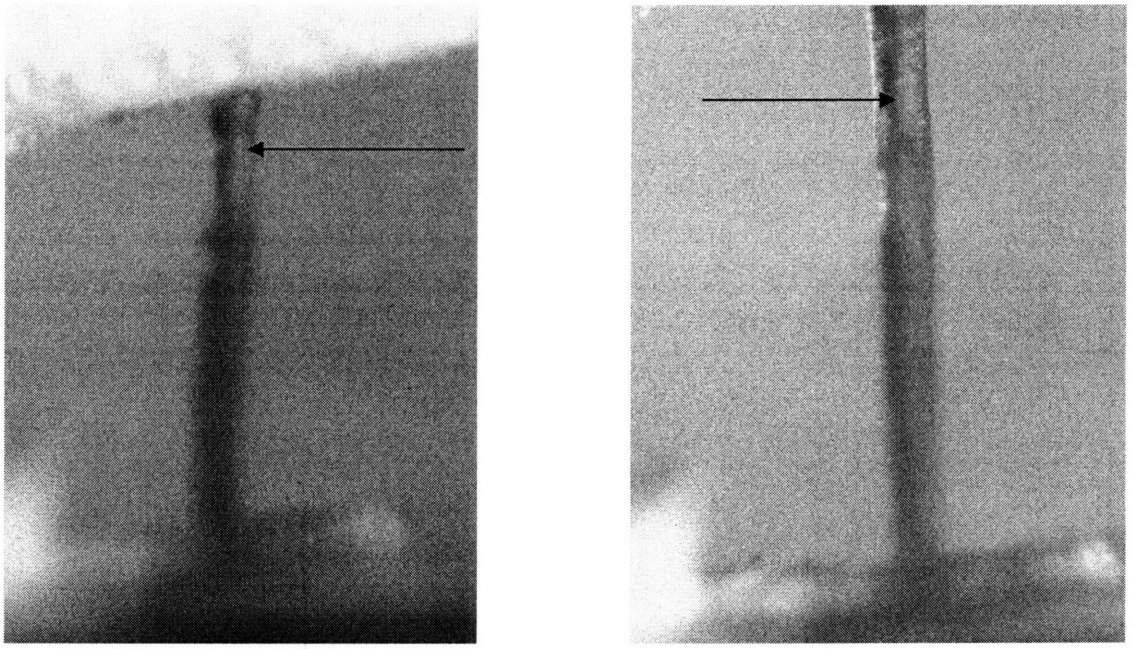

(1) (2)

Figure 2.11: Core section of proximal byssal threads at different strains. The arrows highlight the core, which appears darker relative to the rest of the thread. (1) depicts the thread at a nominal strain of approximately 0.2, while (2) depicts the thread at a nominal strain of approximately 1.5.

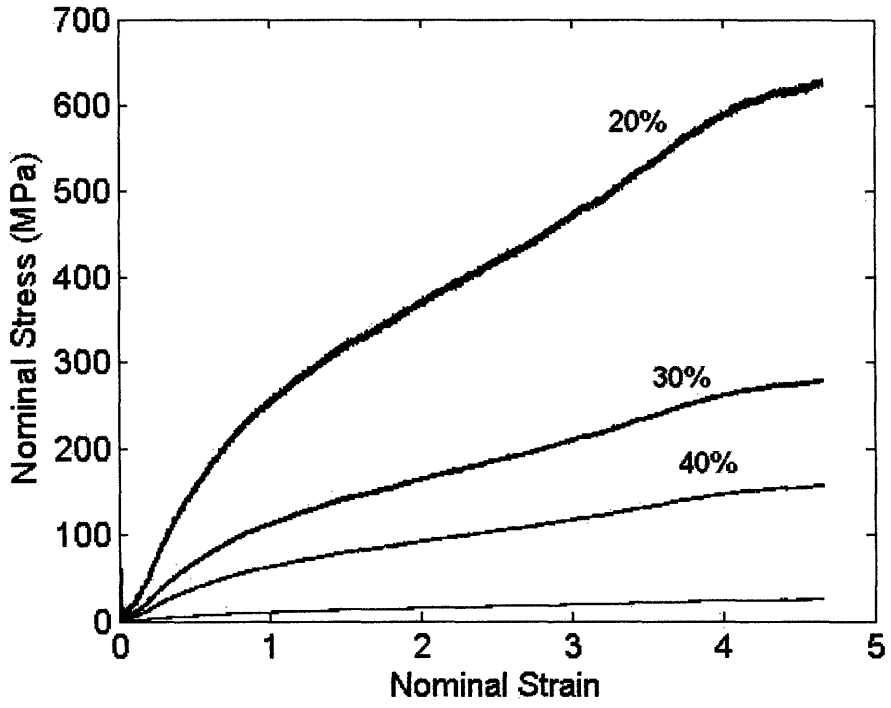

Figure 2.12: Proximal byssal threads in tension to failure at a nominal strain rate of 0.1/s. Curves using different approximations for the inner core diameter are shown. Note that the 30% curve will be used throughout the remainder of this thesis, as that most accurately represents the average value of core diameters for specimens investigated in this thesis.

This is noticeable in the cyclic tests as well.

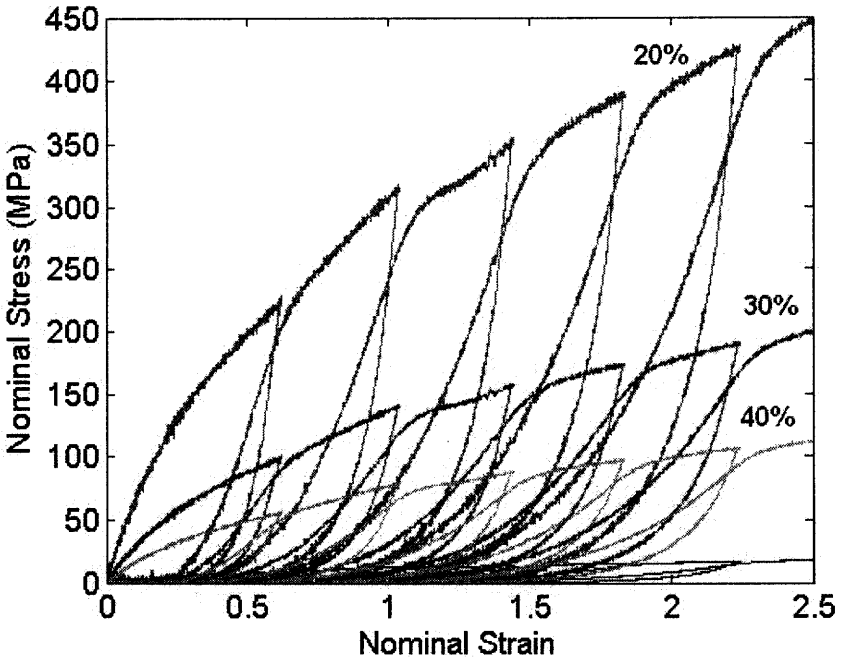

Figure 2.13: Proximal byssal threads in cyclic tension loading at a nominal strain rate of 1/s. Curves using different approximations for the inner core diameter are shown.

It is striking how different the results are between these two cases. For now it is important to realize that the proximal thread's stiffness is not exact, but rather depends on what is considered load-bearing. If only the inner core is considered to be load bearing, then the proximal modulus is much stiffer than the previous literature demonstrates. In this investigation, the thread portions were not separated, but it would be important to see if that is possible and to see how the inner core behaves separate from the surrounding sheath, and to see how the sheath behaves when tested by itself. These results will be compared to results from tests on the distal thread section in section 2.3 of this thesis. The comparison is quite striking.

2.2.2 Distal Behavior

The distal thread section was also tested (separate from the proximal section). These threads showed a behavior quite different from that seen above, though the major deformation mechanism (filament unbending, stretching, and unfolding) is taken to be the same.

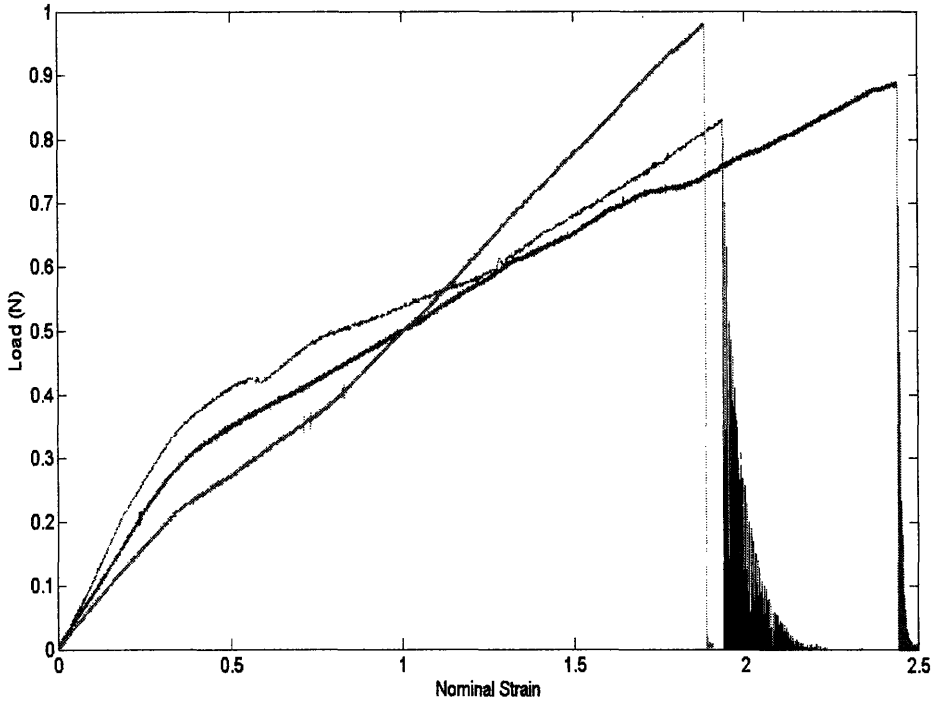

Figure 2.14: Load vs. nominal strain for distal byssal threads at varying strain rates (1/s-top curve, 0.1/s-middle curve, and 0.01/s-bottome curve).

As can be seen in Figure 2.14 the yield in the distal threads occurs at relatively large strains $(\varepsilon \approx 0.4)$ and, at the higher strain rates, is much sharper than that seen in the proximal section. Further, the slope of the thread post yield is much more uniform. The threads also fail at a smaller strain level and the overall stress throughout the test is much higher than in the proximal section. In spite of these differences, the overall shape of the curves is similar to that in the proximal section and can be explained well by the unbending/unfolding criterion discussed previously. Nominal stress vs. nominal strain curves as well as true stress vs. true strain curves were also plotted to allow for better comparison with the proximal section.

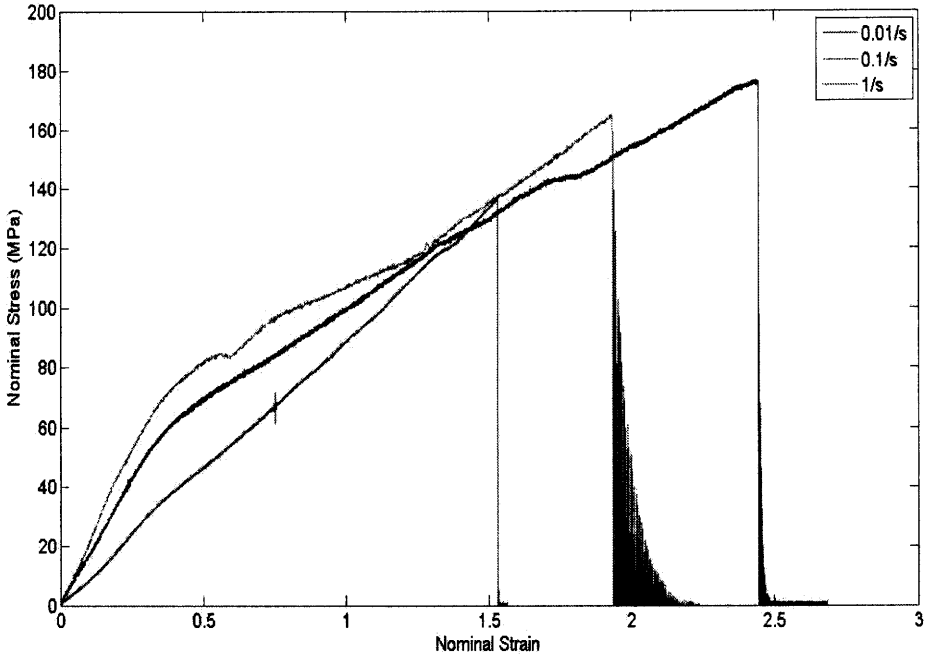

Figure 2.15: Nominal stress vs. nominal strain for distal thread sections. The bottom curve corresponds to the test at a strain rate (nominal strain rate) of 0.01/s, the middle curve corresponds to a strain rate of 0.1/s, and the top curve corresponds to a strain rate of 1/s.

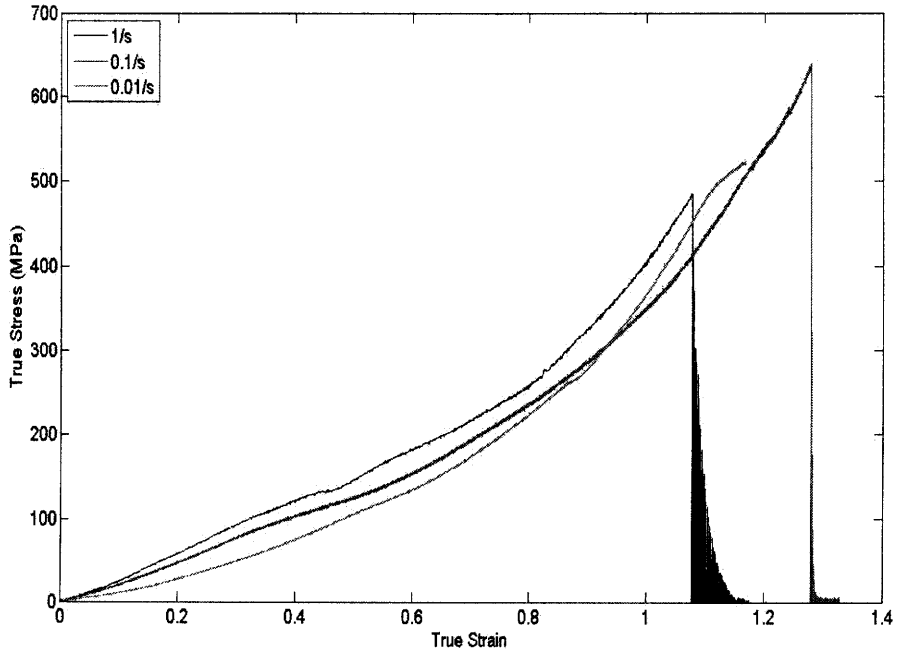

Figure 2.16: True stress vs. true strain for distal byssal threads at varying strain rates.

Cyclic tests were also run on the distal thread sections, to see if the thread behavior was similar to that seen in the proximal section.

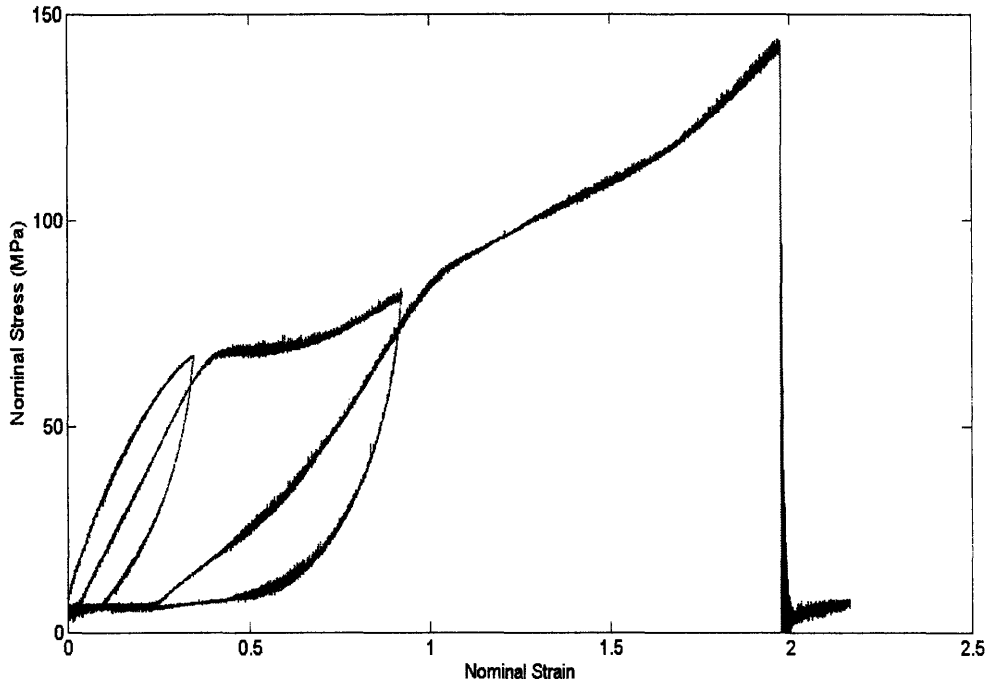

Figure 2.17: Nominal stress vs. nominal strain for cyclic loading of distal thread section. The rate of the test was 0.1/s, and no hold was used between cycles.

As can be seen in Figure 2.17, the reloading curves neither follow the initial loading curves nor follow the unloading curves. This same behavior is however seen in the proximal thread section, so it can be reasonably assumed that the refolding behavior is here also time dependent.

There are three quite interesting points here in examining the cyclic loading curves. First, the difference in recovery between the reloading at low strain $(\varepsilon \approx 0.2)$ and the reloading at high strain $(\varepsilon \approx 1)$ is quite striking. At high strain there is much more recovery, with the curve appearing to arch up, coming much closer to "mirroring" the behavior of the initial loading. Second, the material is much more compliant at the higher strain. The stress increase happens over a much larger strain interval, and is much more gradual. Instead of a quick increase in stress with a small interval of strain, the stress slowly increases at first, before rising more sharply. This behavior is dissimilar to the proximal region, which demonstrated a reloading curve, whose shape was extremely similar to that of the unloading curve. Third, the cyclic curve flattens out much more after yield (than the proximal) i.e. there is an initial elastic response followed by a yield, but after yielding the slope of the loading curve is not straight but rather curves up in an almost exponential fashion. Another way to look at this is that the yield is not sharp (happens quickly), but rather elongated (happens over an extended period of time). This behavior was not

noticed in the proximal threads, and can be better seen by looking at the distal test to failure overlaid with the distal cyclic test.

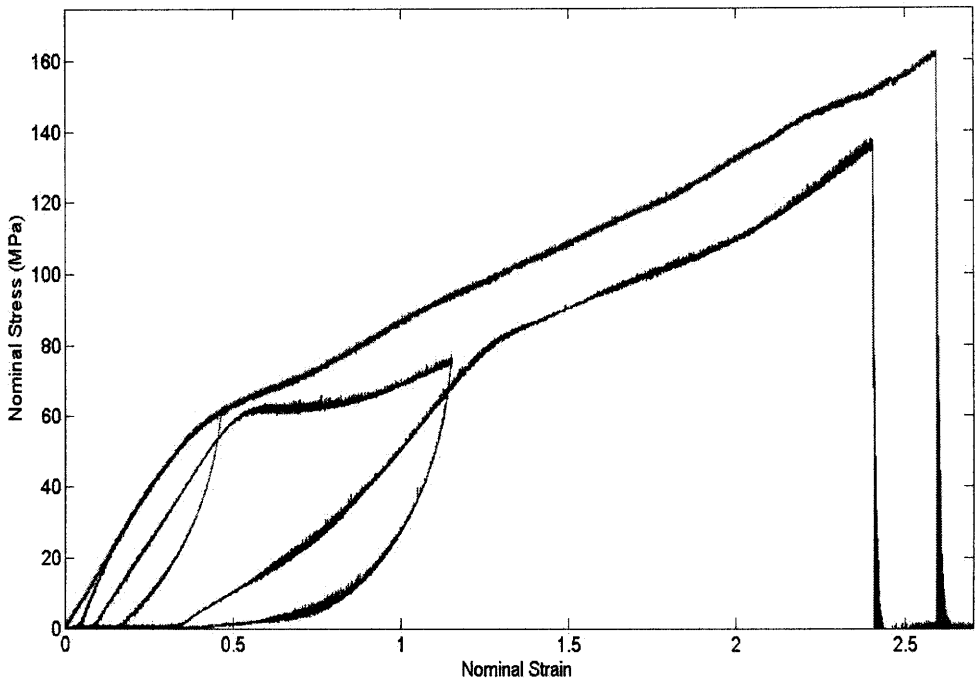

Figure 2.18: Distal thread section cyclic results overlaid with the results of the test to failure. As can be seen, after yield in the cyclic test there is an extra softening before the slope of the cyclic curve turns up (usually corresponding to hardening). The rate of the tests was 0.1/s.

This seemingly strange behavior can be explained by looking at the unbending/stretching/unfolding criterion discussed previously. As was previously discussed, the yield occurs when the weakest secondary bonds are broken and the folded regions begin to unfold. If however, the thread is unloaded as soon as these first bonds break, the filaments will try to refold upon unloading. Again, it is impossible that these bonds reform perfectly, and instead several bonds of approximately equal strength will form. When the thread is then reloaded and the material comes to yield, instead of a sharp yield, several bonds of the same strength will begin to break and a prolonged stretch of approximately equal force will be seen in the subsequent loading curve. This will happen any time that the thread is unloaded and reloaded without reaching full yield.

2.3 Comparing the Proximal and Distal Thread Sections

At first glance, a comparison of the nominal stress-strain curves of the proximal and distal sections shows that the distal section is indeed much stiffer than the proximal section (as is noted in the previous literature) (Carrington and Gosline 2004).

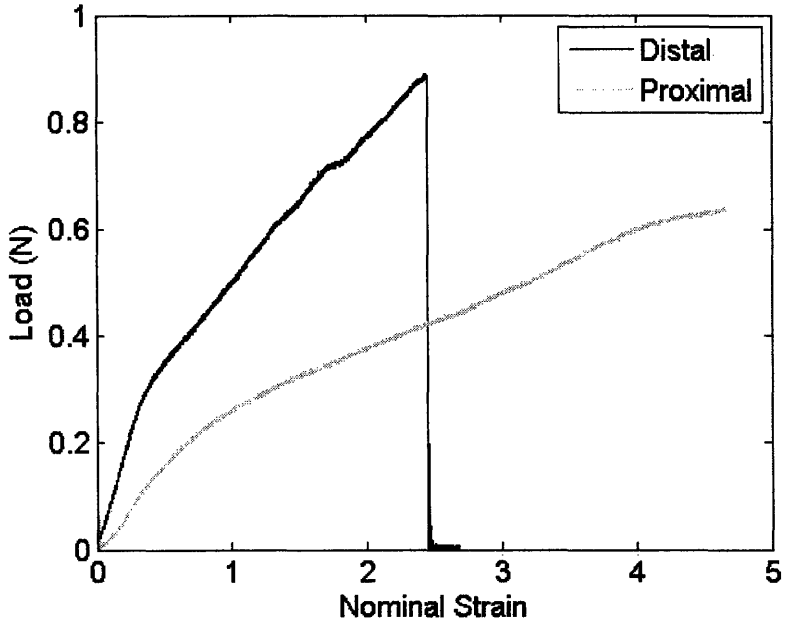

Figure 2.19: Load vs. nominal strain for proximal and distal byssal thread at a nominal strain rate of 0.1/s.

Indeed, at a given load, the proximal thread will deform much more than the distal. For example at a load of 0.2N, the distal thread has only deformed to a nominal strain of approximately 0.25, whereas the proximal thread has deformed to a nominal strain of approximately 0.8. This phenomenon only becomes more exaggerated as the deformation increases. This is highlighted in the following figure (Figure 2.20) which shows load vs. nominal strain for the proximal and distal thread sections, but with horizontal bars drawn in, demonstrating the disparity between the two sections in strain at given loads. These horizontal bars become quite large at larger values of load, with the highest, drawn at approximately 0.55N, being approximately 2.5 nominal strain units in length. These results also indicate that, although the distal region experiences dramatically less strain for any given axial load, it is strained sufficiently to initiate its unfolding once the proximal region exceeds proximal nominal strains of approximately 1.8.

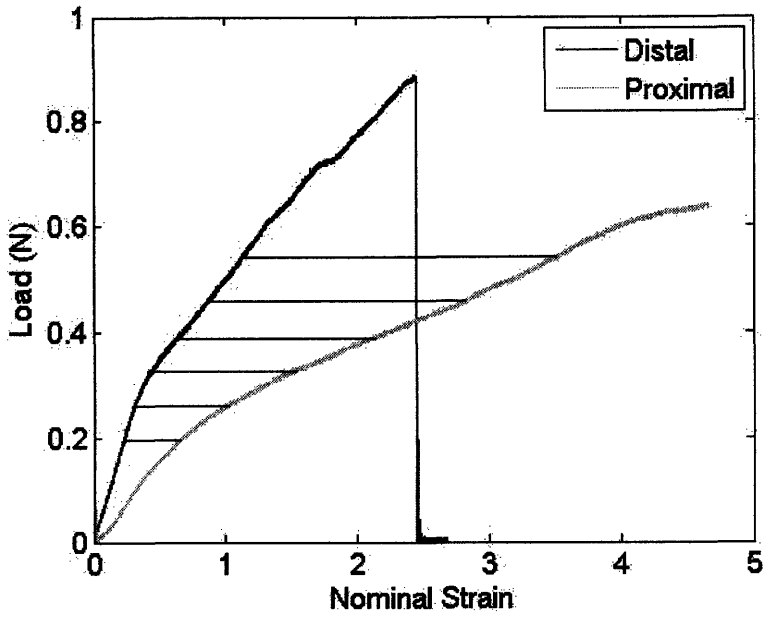

Figure 2.20: Load vs. nominal strain for proximal and distal byssal thread at a nominal strain rate of 0.1/s. Lines connecting the two curves are horizontal and correspond to levels of constant load.

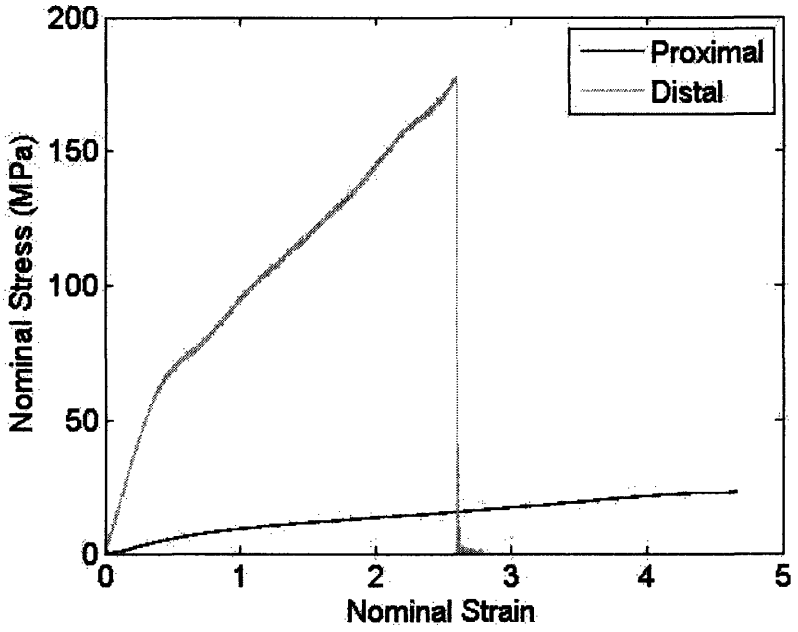

Figure 2.21: Proximal and distal byssal thread sections to failure at a nominal strain rate of 0.1/s. The diameter used for the proximal thread section is the entire diameter.

As can be seen in Figure 2.21, this phenomenon is even more exaggerated when we look at the data in terms of nominal stress instead of load. The proximal thread is far more compliant, deforming to much higher strains at lower stress levels. In fact, the proximal

section is so much more compliant that it fails at a stress that is approximately 6 times lower (failing at approximately 30MPa as opposed to 175MPa). Similarly, the strain at failure is much higher (failing at a strain of approximately 4.5 as opposed to 2.5).

However, this plot uses the entire cross-section of the proximal thread, and because of that the proximal and distal curves are extremely separate on the plot. Therefore, the proximal curve can not be seen in enough detail to truly compare the section behaviors. A more interesting result can be seen when the distal thread is compared to the proximal thread using the proximal thread's inner core as its entire diameter.

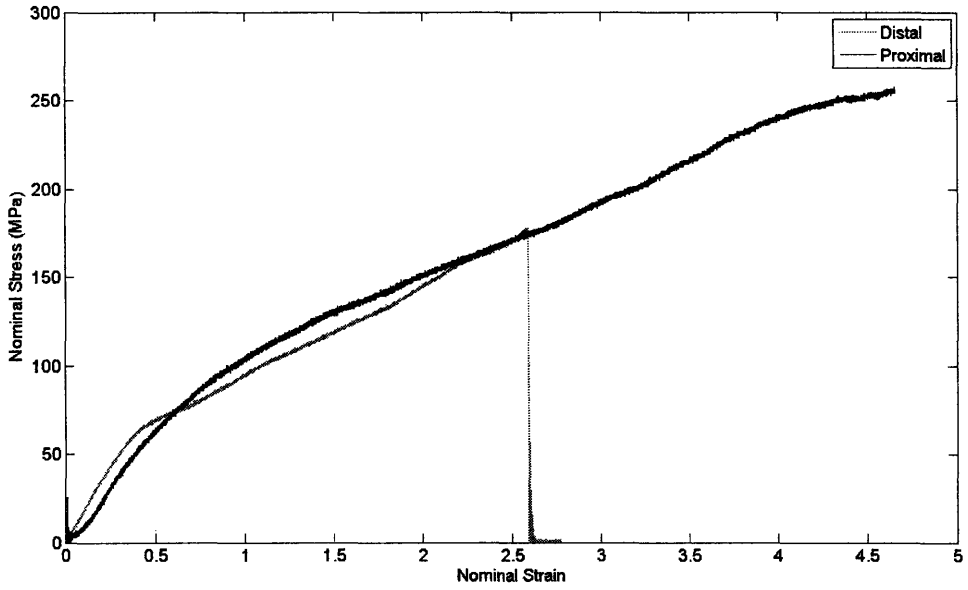

Figure 2.22: Proximal and distal byssal thread sections to failure at a nominal strain rate of 0.1/s. The diameter used for the proximal thread section is the inner core diameter.

Here the nominal stress-strain curves line up much better and full details can be seen for both curves. The values of stress for a given strain appear to be quite similar in both thread sections. However the yield is different; in the distal section, the yield is much sharper, whereas it appears to be more of a "rollover" yield in the proximal section, as if the structural evolution is more controlled and ongoing in the proximal thread, whereas it is sharper and more sudden in the distal.

The similarity in the proximal and distal material stress-strain behaviors suggest that their basic structure is quite close (and perhaps in this species the filament alignment in the proximal may not be "random" but rather well-aligned or there may be a higher density of filaments). It also indicates that the axial gradient in the geometric stiffness (AE as opposed to the material stiffness E) as one travels from proximal to distal is primarily a result of decreasing core diameter.

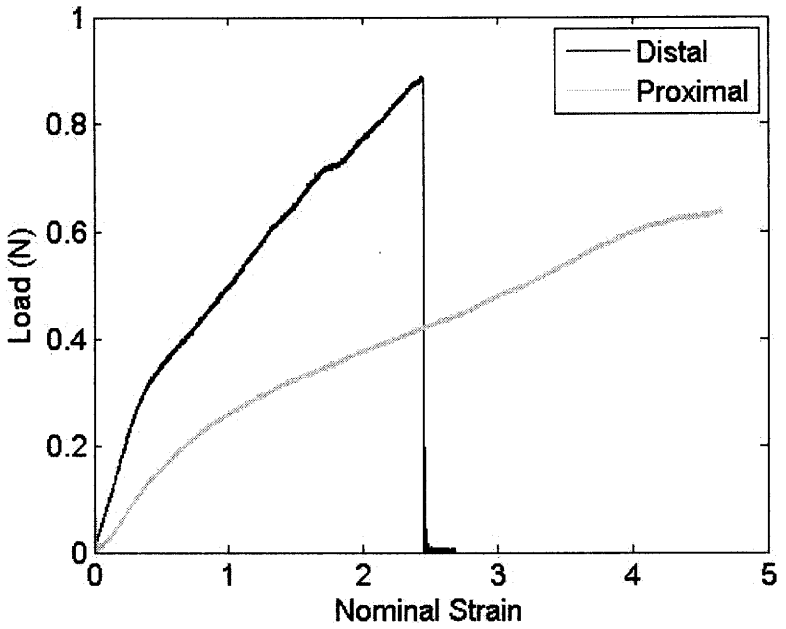

Figure 2.23: Proximal and distal thread sections load vs. nominal strain at a nominal strain rate of 0.1/s. Here again a striking difference between the yield in the proximal section and the yield in the distal section is evident.

This discrepancy in yield behavior between the proximal and distal thread sections is most likely a result of the alignment of the filament bundles. Noting that the filaments are in the direction of the thread axis for the distal section and randomly oriented in the proximal, it makes sense that the distal thread would be stiffer, and demonstrate a more sudden yield. As the distal section is stretched, the unfolding would occur at smaller macroscopic axial strain, because all the travel would be in the direction of the bundles, unbending them and stretching them at all times. In the proximal section, bundles would be aligning (rotating towards tensile axis) as well as unbending and stretching while others are being pulled into alignment with the thread axis, so it would take longer to unfold all sections, thus a more continuous yield phenomenon.

Chapter Three: Modeling

3.1 Constitutive Model of Filament

The deformation of a filament bundle in simple tension will be approximated to follow a conventional axial bar tension behavior where an axial deformation (δ) is applied to the filament, giving rise to a load (P). This follows Equation 3.1

$$P = \frac{A_c E}{L}\delta \tag{3.1}$$

where A_c is the cross-sectional area of the filament bundle, E is the Young's Modulus of the filament bundle, and L is the initial length of the repeat unit of the filament bundle. Thus, as the deformation increases, the load also increases. This deformation is normalized to a nominal axial strain:

$$\varepsilon^{total} = \frac{\delta}{L} \tag{3.2}$$

which, in a conventional metal or plastic, is simply the sum of an elastic strain component and a plastic strain component.

$$\varepsilon^{total} = \varepsilon^{elastic} + \varepsilon^{plastic} \tag{3.3}$$

However, the mussel filaments are not a conventional material, in that their deformation cannot be understood in terms of a traditional elastic and plastic component. Rather, their deformation is the result of a progressive and ongoing structural evolution, which arises from the unbending, stretching, and unfolding of the filament bundles.

Here will be discussed the deformation of the filament bundles with respect to stretching and unfolding (unbending is neglected).

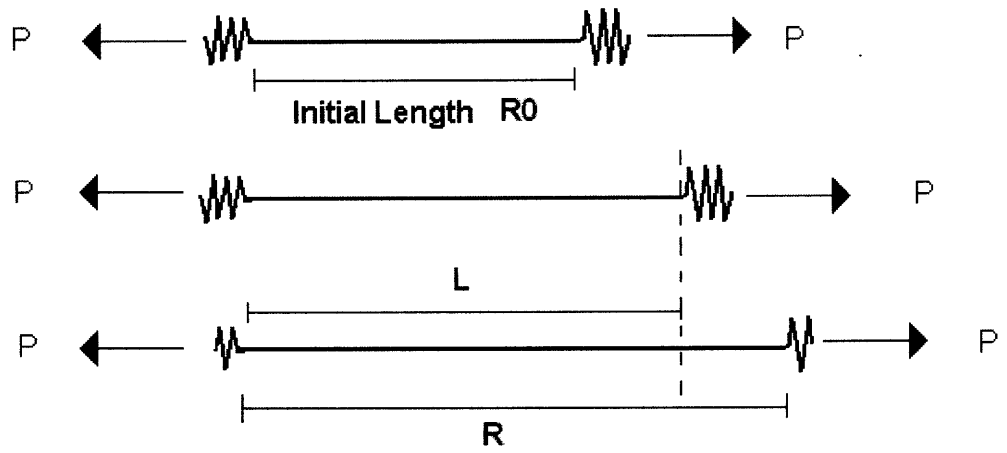

Figure 3.1: Filament deformation without unbending. Here, R is taken to be the overall length of the filament while L is taken to be the tension-free length.

Thus, the load and displacement of the filament can be modeled similar to a beam in tension except that when the folded domains begin to unfold they provide additional tension-free length. The rate of this unfolding can be modeled using an Eyring model as adapted by Bertoldi and Boyce (2007), and is a function of the load on the fiber (P), the Boltzmann Constant (K), temperature (θ), an external lumped parameter (α), and the width of the activation barrier (x_A), giving an expression for the rate of increase in the tension-free length of the filament repeat unit:

$$\dot{L} = \alpha(L_{\max} - L_t)\exp\left[\frac{Px_A}{K\theta}\right] \tag{3.4}$$

Note that the term $(L_{\max} - L_t)$ acts in two ways: (1) to increase the force needed to increase L at a given rate, and (2) to provide a saturation length given that there will be some limited length available in the folded domains. It is also important to note that the rate of overall thread stretching (both tension and tension-free lengths) is a function only of the imposed nominal strain rate ($\dot{\varepsilon}$) and the initial length of the bundle (R_0).

$$\dot{R} = R_0 \cdot \dot{\varepsilon} \tag{3.5}$$

The evolution of length (tension-free $L_{(t+\Delta t)}$ and overall $R_{(t+\Delta t)}$) can be easily determined from these parameters.

$$R_{(t+\Delta t)} = R_0 + \dot{R}\,\Delta t \tag{3.6}$$

$$L_{(t+\Delta t)} = L_t + \dot{L}\,\Delta t \tag{3.7}$$

With these parameters known, it becomes possible to determine the load on the filaments, since it is known that the load is a function only of the cross-sectional area (A) (approximated as constant) and Young's Modulus (E), and of the filament stretch as demonstrated above.

$$P = \frac{AE}{L_{(t+\Delta t)}}\left(R_{(t+\Delta t)} - L_{(t+\Delta t)}\right) \tag{3.8}$$

Multiplying the outer term and dividing the bracketed term by R_0 gives a more useful form of the equation, namely one that is in terms of stretch $\lambda_f = \frac{R}{R_0}$.

$$P = \frac{AER_0}{L}\left(\lambda_f - \frac{L}{R_0}\right) \tag{3.9}$$

The usefulness of this form of the equation will become more apparent in the following sections.

These equations were solved simultaneously using a Forward Euler Integration in Matlab. The results were plotted for the bundles with unfolding and without unfolding. As can be seen in Figure 3.2 initially the two curves follow the same path corresponding to the time before which any unfolding has occurred. As the deformation increases, unfolding occurs and the load on the fiber with unfolding is less at a given deformation than that without unfolding.

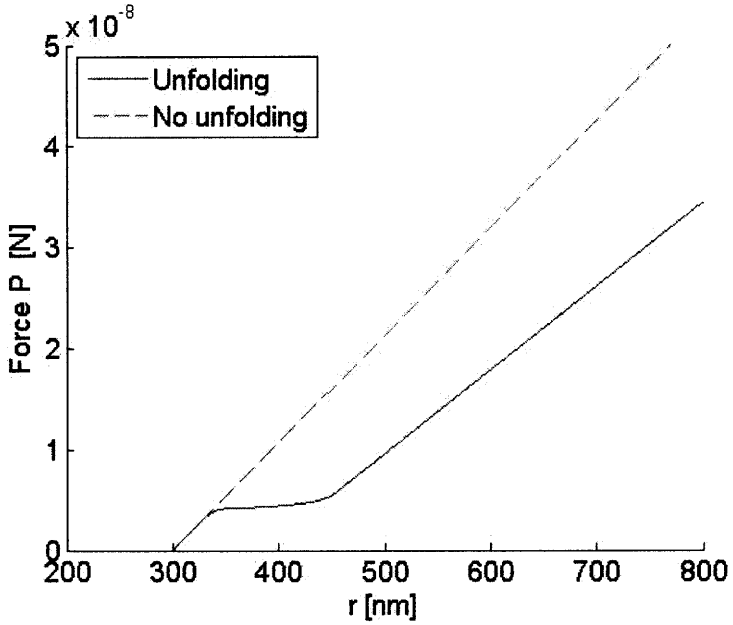

Figure 3.2: Demonstration of load on fiber bundles with unfolding of the folded ends taken into account and without unfolding. As can be seen the load for the case of unfolding follows the case with no unfolding initially, corresponding to a time before unfolding occurs. Then, the unfolding curve is lower.

This Matlab simulation was also used to investigate the progression of the unfolding as the deformation increased. Obviously there is some finite amount of stored length in the folded regions of the filaments (the L_{max} term in Equation 3.4). Thus, when all the folded regions unfold, the tension-free length (the intial unstretched length of the filament plus the length added via unfolding) comes to some steady-state value. This is seen in Figure 3.3 (2).

Initially, the tension-free length is constant, as no folded domains have unfolded, releasing extra tension-free length. However, as the deformation increases, the folded domains begin to unfold. When all the unfolded domains unfold, the amount of tension-free length again comes to a steady state value (the L_{max} in Equation 3.4, which is here taken to be 385nm). Figure 3.3 depicts these images side by side, to make the relationship between load and unfolding clearer.

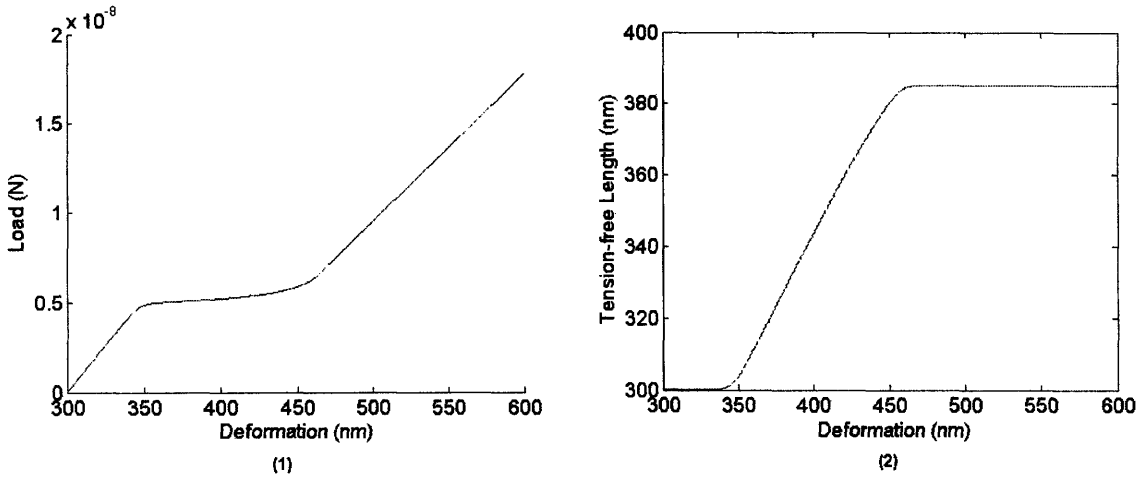

Figure 3.3: (1) Load vs. deformation for simulation of loading a filament bundle. (2) Tension-free length vs. deformation for simulation of loading a filament bundle. Initially when there is no unfolding, the load on the bundle increases quickly. As unfolding occurs (deformation of roughly 345nm to 450nm) the load increases very slowly. When unfolding stops (all of the bundle's folded domains have unfolded) the load on the bundle again increases quickly.

This unfolding is rate-dependent, as is seen in Figure 3.4. As the imposed rate of deformation increases, a higher force is required to initiate unfolding and hence it initiates at slightly larger strain as well. This can be easily understood by looking at the extreme case of stretching the thread immediately (an infinitely high rate). In this case, there would be no time for the folded regions to unfold and the tension-free length would remain at 300nm (the initial value). Thus, as the rate increases the amount of deformation required to reach a given tension-free length also increases.

Once unfolding begins, the shape of the curve is quite similar, and the final value of tension-free length is the same (385nm) regardless of rate. This is true because the maximum amount of length in the folded domains is a material property and not dependent on the rate of the test.

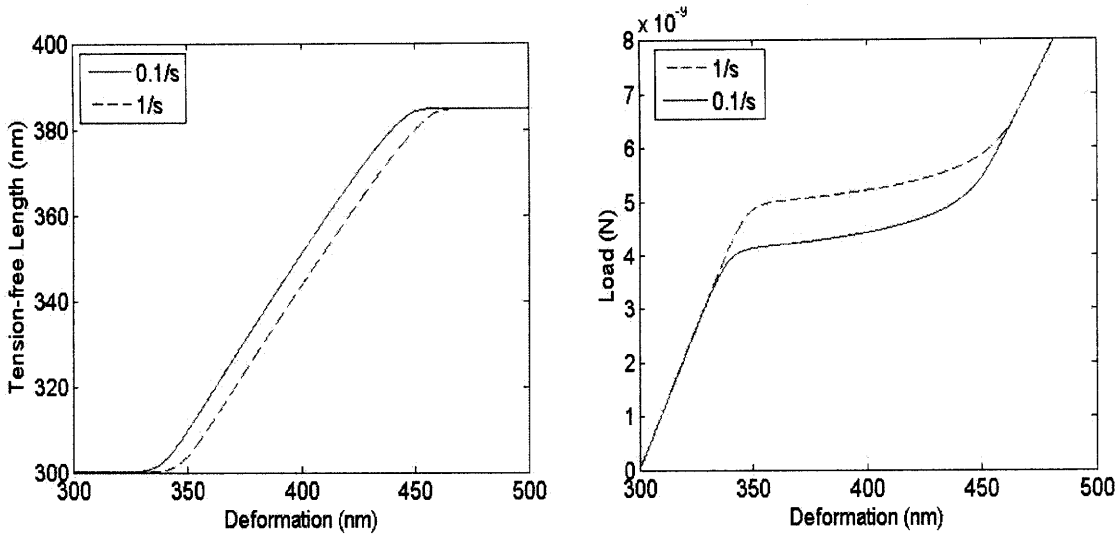

Figure 3.4: Tension-free length vs. deformation (left) and load vs. deformation (right) for model's simulation of loading on filament bundles at different strain rates.

Similarly, the loading vs. deformation plot is rate-dependent. At higher rates, the magnitude of the load plateau is larger, because the plateau occurs at higher deformations. This can be understood by noting that when the bundle deforms (prior to unfolding) the already straight domains of the bundles stretch. Via Equation 3.1, if δ increases at a given value of L then P must also increase.

As a final note, it is important to investigate the behavior of the thread in loading, unloading, and reloading.

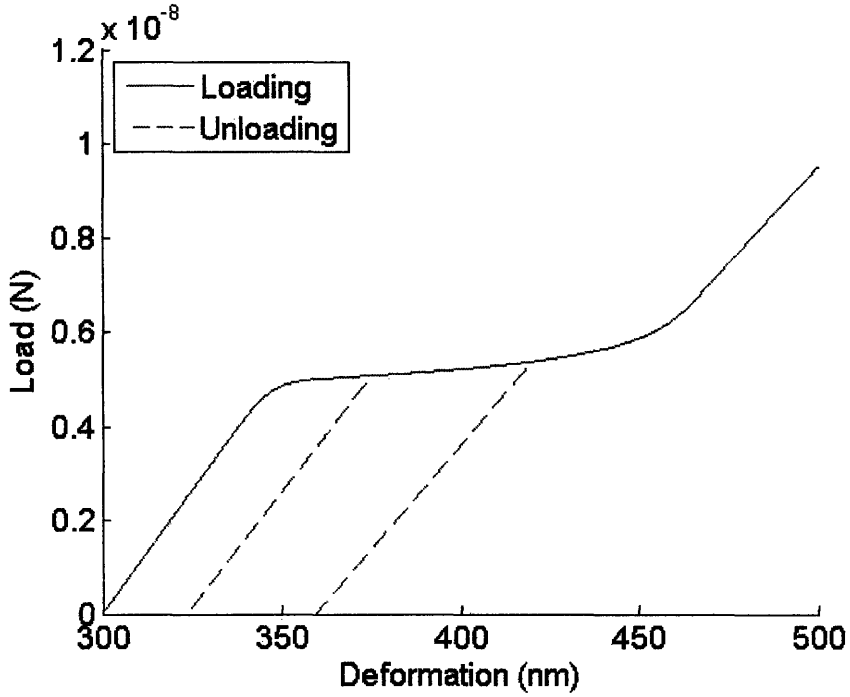

Figure 3.5: Simulation of loading/unloading/reloading of filament bundles. Simulation was run for a nominal strain rate of 1/s.

In this case, refolding of filament bundles was neglected. Since the refolding is time-dependent, this assumes that this is a high enough strain rate such that refolding during unloading does not occur. It also assumes no hold-time in between the unloading and reloading. Note that the reloading curve follows the unloading curve, and that the unloading curve follows the x-axis when it reaches a load of 0N. Note the difference in slope of the two unloading curves. This is because at higher strains more filaments have unfolded, providing more tension-free length, which directly influences the Load, and gives a more compliant behavior as evident in the lower slope upon reloading. When the reloading behavior reaches the initial curve, the reloading curve then travels with what would have been the monotonic curve.

3.2 Strain Evolution on the Macrosctructure

3.2.1 Work Density of the Neo-Hookean Matrix and Fiber Bundles

Once the force-extension behavior of the bundles is determined, it can be used to construct a stress-strain relationship for the entire thread, where the volume of the gel-like matrix surrounding these fiber bundles can be approximated as a Neo-Hookean material. The fiber bundles themselves serve to stiffen this matrix, and so the work density of the matrix sums with the work of the individual fibers multiplied by the density of fibers within the thread. This can then be used to determine the stress-strain behavior of the thread itself.

$$W_{total} = W_{matrix} + n * w_{fiber} \tag{3.10}$$

where n is simply the number density of the fibers within the thread.

Assuming that the matrix is an incompressible Neo-Hookean material, the work density is given by:

$$W = C\left(\lambda_1^2 + \lambda_2^2 + \lambda_3^2 - 3\right) \tag{3.11}$$

where the $\lambda_i (i = 1,2,3)$ correspond to stretch ratios in the three principal directions. The incompressibility assumption requires that the different stretch ratios be related.

$$\lambda_1 \lambda_2 \lambda_3 = 1 \tag{3.12}$$

For cases where loading is symmetric about the 1-axis:

$$\lambda_2 = \lambda_3 = \frac{1}{\sqrt{\lambda_1}} \tag{3.13}$$

because in such cases the stretches in the 2 and 3 directions are equal. Equation 3.13 holds for this case of uniaxial tension, because the loading is symmetric about the 1-axis.

The work of the fiber bundles can be determined from the force-extension behavior given earlier. Since these bundles elongate as tension is applied, the work to stretch is simply the integral of the applied force multiplied by the displacement, taken over the entire length of the displacement.

$$w_f = \int P d\delta_f \tag{3.14}$$

Since the evolution of the load as a function of displacement was determined above, Equation 3.8 can be inserted into Equation 3.14 as well as a term for the displacement with respect to known quantities (R and L), yielding Equation 3.15.

$$w_f = \int \frac{EA}{L}(R - L) \cdot d(R - L) \tag{3.15}$$

Equation 3.15 is integrated to determine the work of the fiber bundle. The corresponding equation is then rearranged to give the work as a function of fiber stretch $\lambda_f = \frac{R}{R_0}$.

$$w_f = \frac{1}{2} EA \frac{R_0^2}{L}\left(\lambda_f - \frac{L}{R_0}\right)^2 \tag{3.16}$$

where R_0 is the initial length of the bundle. The contribution of the fibers to the work density of the thread is then the product of the work of a fiber bundle and the number of fiber bundles per unit volume of thread n or $W_f = nw_f$.

3.2.2 Mapping Thread Stretch to Fiber Stretch Using Directionality of Fiber Bundles

However, Equation 3.15 gives the work as a function of fiber stretch, whereas the equation for the work density of the matrix is in terms of the macroscopic stretches in the principal directions. Before the total work density can be evaluated, these equations must be reconciled. So, it is approximated that the fibers deform affinely with the matrix. This approximation determines the relationship between the fiber stretch and the macroscopic principal stretches. In order to determine an expression for this relationship, linear algebra is employed, noting that in the distal thread section the fibers align parallel to the thread axis, whereas in the proximal thread section the fibers orient randomly.

It is first noted that the stretch in the direction of the fiber is related to the right Cauchy-Green tensor

$$\lambda_f = \mathbf{A} \cdot \mathbf{CA} \tag{3.17}$$

where,

$$\mathbf{C} = \mathbf{F}\mathbf{F}^T \tag{3.18}$$

and where **F** is the deformation gradient, which for this case (the case without off-diagonal shears and without rotation) is simply:

$$\mathbf{F} = \begin{bmatrix} \lambda_1 & 0 & 0 \\ 0 & \lambda_2 & 0 \\ 0 & 0 & \lambda_3 \end{bmatrix} \tag{3.19}$$

giving:

$$\mathbf{C} = \begin{bmatrix} \lambda_1^2 & 0 & 0 \\ 0 & \lambda_2^2 & 0 \\ 0 & 0 & \lambda_3^2 \end{bmatrix} \tag{3.20}$$

And where $\boldsymbol{A}$ is the unit vector direction of the fiber bundle. In the distal thread section the direction vector ($\boldsymbol{A}$) is simply [1 0 0]. Thus, the fiber stretch can be related to the macroscopic principal stretches by:

$$\lambda_f = \lambda_1 \tag{3.21}$$

This however is not the case in the proximal thread section. Since the fiber bundles in the proximal thread section are randomly aligned, no single vector can be used to encompass every fiber. Therefore, an average value vector must be used. Here, the Arruda –Boyce 8-chain model is employed, which gives the fiber stretch in terms of the principal stretches as:

$$\lambda_f = \sqrt{\frac{1}{3}\left(\lambda_1^2 + \lambda_2^2 + \lambda_3^2\right)} \tag{3.22}$$

Note for this simple case of uniaxial tension, this is analogous to taking $\boldsymbol{A} = [\frac{1}{\sqrt{3}} \frac{1}{\sqrt{3}} \frac{1}{\sqrt{3}}]$.

3.2.3 Determination of Stress and Strain from Work Density

As given in Equation 3.10, the work densities from the matrix and the fiber bundles sum, giving the total work density of the thread. This total work density is given in Equation 3.23.

$$W = C\left(\lambda_1^2 + \lambda_2^2 + \lambda_3^2 - 3\right) + \frac{n}{2} EA \frac{R_0^2}{L}\left(\lambda_f - \frac{L}{R_0}\right)^2 \tag{3.23}$$

The total work density can then be used to determine the stress on the thread as a function of stretch (and therefore also strain). The following equation, obtaining true stress by differentiating the work density, is employed.

$$T = \lambda_i \frac{dW}{d\lambda_i} - P^* \tag{3.24}$$

Since both the matrix and the fiber bundles are taken to be incompressible, there is an additional hydrostatic term (P^*) which does not do work (hence it does not contribute to W and therefore cannot be found by differentiating W) which is non-zero and must be determined by satisfying equilibrium. This can be done by noting that the true stress in the 2 and 3 directions is zero, since the only load is applied in the 1-direction.

Differentiation of Equation 3.23 yields an expression for the three principal true stresses. This gives a universal expression for T_i:

$$T_i = \lambda_i \left[2C\lambda_i + \frac{\partial}{\partial \lambda_i}\left(\frac{nAE}{2L} R_0^2 \left(\lambda_f - \frac{L}{R_0} \right)^2 \right) \right] - P^* \tag{3.25}$$

Because λ_f is different in the distal and proximal section, the true stress term reduces differently in each case. Noting that $T_2 = T_3 = 0$ and that $\lambda_2 = \lambda_3 = \frac{1}{\sqrt{\lambda_1}}$ the true stress term (T) in the 1-direction (the direction of loading) for the distal section reduces to:

$$T_1 = \lambda_1\left[2C\lambda_1 + \frac{nAER_0^2}{L}\left(\lambda_1 - \frac{L}{R_0}\right)\right] - \frac{2C}{\lambda_1} \tag{3.26}$$

Noting that the fiber length L evolves during deformation due to unfolding, L needs to be determined at each strain via the Forward Euler process discussed above. The calculation was done in Matlab and the results for both the proximal and distal thread sections are plotted below.

Equation 3.25 was also applied to the proximal thread section. Again, noting that $T_2 = T_3 = 0$ and that $\lambda_2 = \lambda_3 = \frac{1}{\sqrt{\lambda_1}}$ the true stress term (T) in the 1-direction (the direction of loading) for the proximal section reduces to:

$$T_1 = \lambda_1\left[2C\lambda_1 + \frac{nAER_0^2}{L}\left(\sqrt{\frac{1}{3}\left(\lambda_1^2+\lambda_2^2+\lambda_3^2\right)} - \frac{L}{R_0}\right)\left(\frac{\lambda_1}{\sqrt{\frac{1}{3}\left(\lambda_1^2+\lambda_2^2+\lambda_3^2\right)}}\right)\right] - P^*_{proximal} \tag{3.27}$$

where:

$$P^*_{proximal} = \frac{1}{\sqrt{\lambda_1}}\left[\frac{2C}{\sqrt{\lambda_1}} + \frac{nAER_0^2}{L}\left(\sqrt{\frac{1}{3}\left(\lambda_1^2+\lambda_2^2+\lambda_3^2\right)} - \frac{L}{R_0}\right)\left(\frac{1}{\sqrt{\frac{1}{3}\lambda_1\left(\lambda_1^2+\lambda_2^2+\lambda_3^2\right)}}\right)\right] \tag{3.28}$$

Inserting equation 3.22, this reduces to:

$$T_1 = \left(2C + \frac{nAER_0^2}{L\lambda_f}\left(\lambda_f - \frac{L}{R_0}\right)\right)\left(\lambda_1^2 - \frac{1}{\lambda_1}\right) \tag{3.29}$$

Noting that fiber length L evolves during deformation due to unfolding, L needs to be determined at each strain via the Forward Euler process described above. The calculation was done in Matlab and the results for both the proximal and distal thread sections are plotted below.

The true stress T_1 is the axial force on the thread divided by its current cross-sectional area A. The corresponding nominal stress N_1 is the axial force divided by the original

cross-sectional area A_0. Assuming incompressibility of the thread deformation and using l for current thread length and l_0 for original thread length gives: $Al = A_0 l_0$. Therefore, $A_0 = \frac{l}{l_0} A$ or $A_0 = \frac{A}{\lambda_1}$ which gives:

$$N_1 = \frac{T_1}{\lambda_1} \tag{3.30}$$

The true axial strain is $\varepsilon_{T1} = \ln\left(\frac{l}{l_0}\right) = \ln(\lambda_1)$; the nominal axial strain is $\varepsilon_{N1} = \frac{l - l_0}{l_0} = \lambda_1 - 1$, which gives:

$$\varepsilon_{N1} = \exp(\varepsilon_{T1}) - 1 \tag{3.31}$$

These equations, 3.30 and 3.31 above, are then used to convert the true stress-true strain curves to nominal stress-nominal strain curves. Results will be presented in both forms.

3.2.4 Determination of Material Parameters

Throughout the above derivation, it was assumed that the values of some important material parameters were known, namely A, E, n, R_0, α, and x_A. Before any simulations could be run using this model, these properties had to be determined.

First n was determined, since this could be determined from looking at micrographs. From Figure 1.5, the number of filaments in a tiny thread section were counted (the tiny dark streaks correspond to a single filament bundle). Assuming that this section is indicative of an entire thread and that this image depicts a slice taken directly along the central axis of a thread that is 0.8mm in diameter (the average for distal threads), a crude approximation for the fiber density was determined. This number was taken to be approximately 1×10^{20} m^{-3}.

R_0 and A were also determined from previous literature. Hassenkam et. al. (2004) give the length of the unbent filaments to be 300nm, and the diameter of the bundles to be 9nm. Approximating the cross-section of the filament as circular, this gives a cross-sectional area of 1.0179×10^{-15} m^2.

E can be determined from the slope of the true stress vs. stretch plot, but first the equation for true stress must be differentiated in terms of the fiber stretch. For the distal section the fiber stretch is equal to the stretch in the 1-direction, so the derivative becomes:

$$\left(\frac{\partial T_1}{\partial \lambda_1}\right) = 4C\lambda_1 + nAER_0(2\lambda_1 + 1) \tag{3.32}$$

Evaluating this equation at $\lambda_1 = 1$ i.e. a value of stretch small enough that significant yielding has not occurred, the equation reduces to:

$$\left(\frac{\partial T_1}{\partial \lambda_1}\right)\Bigg|_{\lambda_1=1} = 4C(1) + nAER_0(2*1+1) \tag{3.33}$$

From experimental results, this slope was determined to be approximately 56 MPa (tests at the intermediate strain rate of 0.1/s were used):

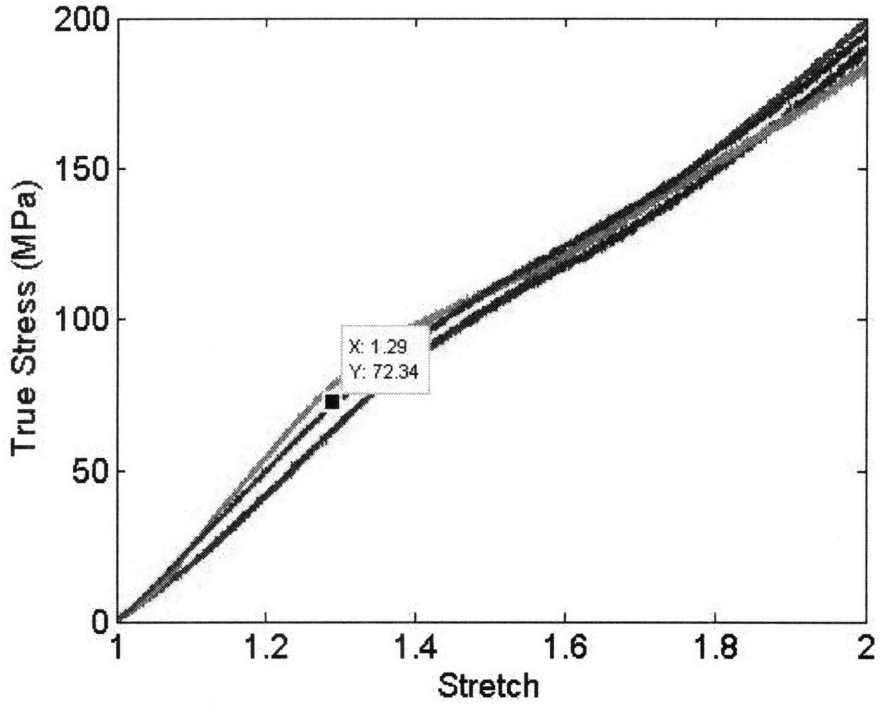

Figure 3.6: True stress vs. stretch for distal byssal threads at a strain rate of 0.1/s.

Using the above values for n, E, and R_0, and using a "small" value for C since C is the matrix shear modulus divided by 2, and the matrix shear modulus in this case is very small (say C = 0.5MPa) compared to the modulus contribution from the filaments, E was determined to be approximately 0.5GPa.

For the proximal section, the differentiation is more difficult, because the fiber stretch in terms of the stretches in the principal directions is the more complicated relation given in Equation 3.22. The differentiation reduces to:

$$\left(\frac{-9nAER_0^2\lambda_1\left(\frac{1}{3}\sqrt{\beta}-\frac{L}{R_0}\right)}{L\beta^{\frac{3}{2}}}+\frac{3nAER_0^2\lambda_1}{L\beta}\right)\left(\lambda_1^2+\frac{1}{\lambda_1}\right)+\left(2C+\frac{3nAER_0^2\left(\frac{1}{3}\sqrt{\beta}-\frac{L}{R_0}\right)}{L\sqrt{\beta}}\right)\left(2\lambda_1+\frac{1}{\lambda_1^2}\right) \tag{3.34}$$

where

$$\beta=3\lambda_1^2+\frac{6}{\lambda_1} \tag{3.35}$$

Again, this differential is evaluated at a small value of stretch, noting that A and R_0 are the same as in the distal section. The variables C, n, and E however need to be determined. Assuming that C should stay the same, since the jelly-matrix should not change from proximal to distal section, the only variables are n and E. n however, is not the same, and micrographs of this section are not clear enough to determine the proximal sections fiber density. But, since n and E always appear together, taking them as a lumped parameter is possible. Therefore, it is determined that nE is equal to 4.1×10^{29} Pam^{-3}. Note from the Figure below that the value of the slope was taken to equal 19 MPa.

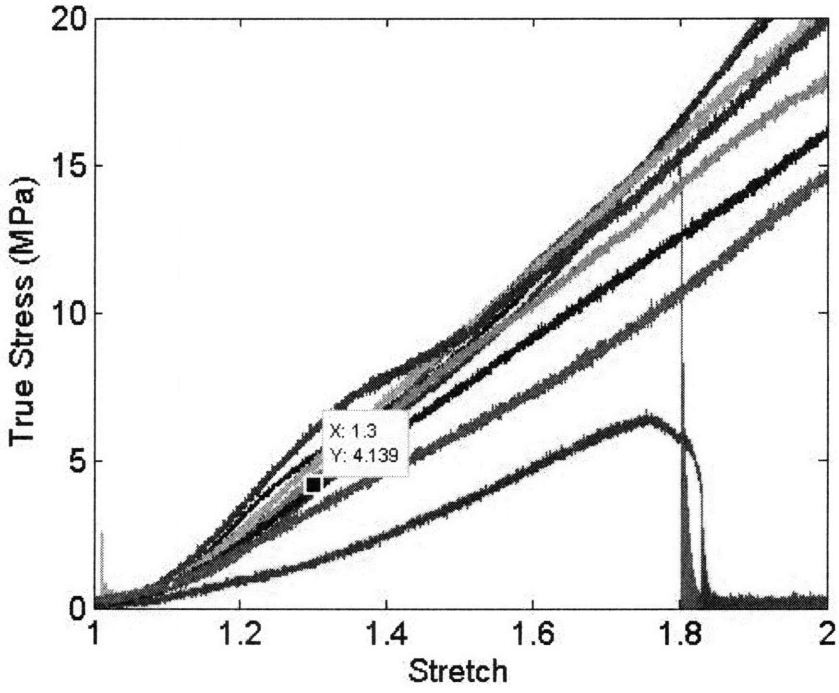

Figure 3.7: True stress vs. stretch for proximal byssal threads at a strain rate of 0.1/s.

Similarly, the final two parameters (α and x_A) can be determined from experimental results. Equation 3.4 can be rearranged such that it forms the equation of a line, whereby load is the y-axis and the natural logarithm of the rate of increase of tension-free length is on the x-axis.

$$Px_A = K\theta \ln\left(\dot{L}\right) - K\theta \ln\left(\alpha\left(L_{\max} - L_t\right)\right) \tag{3.36}$$

Thus, if filament load is plotted against the natural logarithm of the rate of length increase, the result should be a line. The equation for this line can be fit to equation 3.36 and since K and θ are simply the Boltzmann Constant and the absolute temperature of the environment (room temperature) respectively, the values of α and x_A can be determined. There is, however, a problem, namely that we don't know the load as a function of the rate of length increase. However, noting that we do have nominal stress vs. nominal strain plots, it is not hard to convert these into load vs. rate of tension-free length increase using Equation 2.1 to convert between nominal stress and load, and Equation 3.5 to convert between nominal strain rate and rate of increase of tension-free length.

For the distal section, Figure 2.15 (nominal stress vs. nominal strain at varying strain rates) was used to determine two values of nominal stress at two different strain rates. Equations 2.1 and 3.5 were used to convert this to stress and rate of increase of tension-free length. Note also that the value for L_t was taken to be the unstretched length (300nm), since the values for load used were taken prior to significant yield, meaning that very few (if any) folded regions had yet unfolded. This gave two equations and two unknowns. The unknowns were found to be $\alpha = 5.13\times10^{-6}$ s^{-1} and $x_A = 1.1\times10^{-11}$ m. For the proximal section, Figure 2.8 was used. In this case, the unknowns were found to be $\alpha = 4.75\times10^{-4}$ s^{-1} and $x_A = 7.15\times10^{-11}$ m. With all the parameters found, the model could now be employed to characterize the material behavior. The parameters are shown here together:

Table 3.1: Important parameters for modeling.

Distal		**Proximal**	
n [m^{-3}]	1×10^{20}	n	(See E)
A [m^2]	6.4×10^{-17}	A [m^2]	6.4×10^{-17}
E [GPa]	0.5	* nE [GPa*m^{-3}]	4.1×10^{29}
α [s^{-1}]	5.13×10^{-6}	α [s^{-1}]	4.75×10^{-4}
x_A [nm]	.011	x_A [nm]	.0715
C [MPa]	0.5	C [MPa]	0.5
R_0 [nm]	300	R_0 [nm]	300

3. 3 Results of Modeling

3.3.1 Proximal Section

Once the model had been developed, and the appropriate parameters had been determined, the model was input into Matlab, for different loading conditions (monotonic and cyclic at a variety of strain rates). First, simulations for loading of the proximal thread sections to failure were conducted. Figure 3.8 demonstrates the model's ability to predict the nominal stress-nominal strain behavior of the proximal byssal threads.

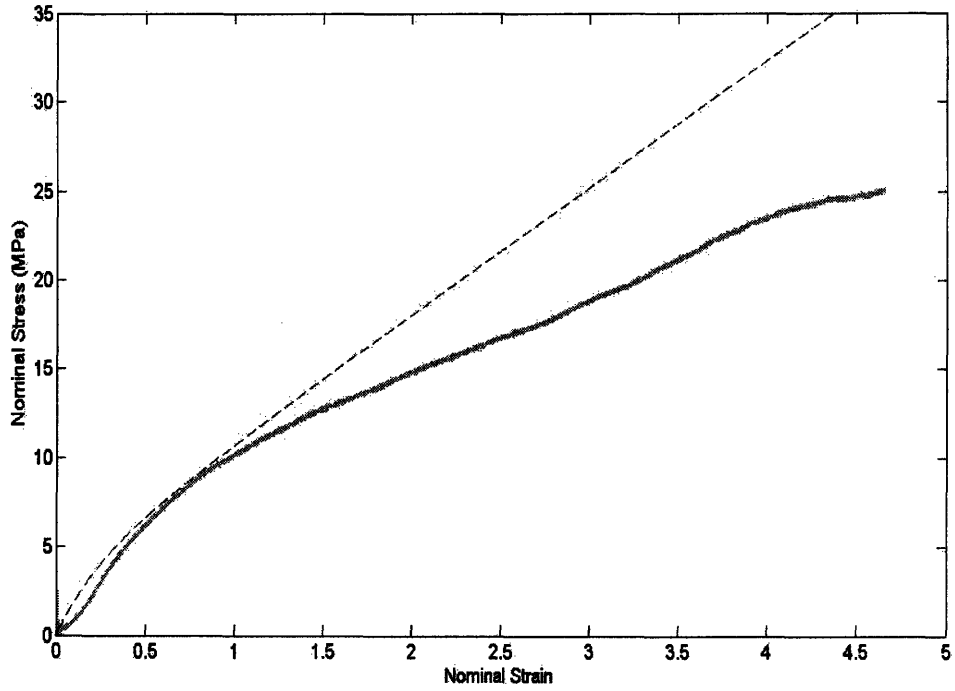

Figure 3.8: Nominal stress vs. nominal strain for proximal byssal threads at a nominal strain rate of 0.1/s. The full line is a curve, which was found to be characteristic. The dashed line corresponds to the model's prediction.

As can be seen in Figure 3.8, the model captures the initial loading behavior of the proximal thread. However, the model is deficient in capturing the full rollover of the yield. Rather, the model predicts a smoother yield, transitioning into another straight region (a behavior that is shown by the thread). However, the slope of this second straight region is higher in the model than in the thread. This can be seen also in looking at true stress-true strain curves.

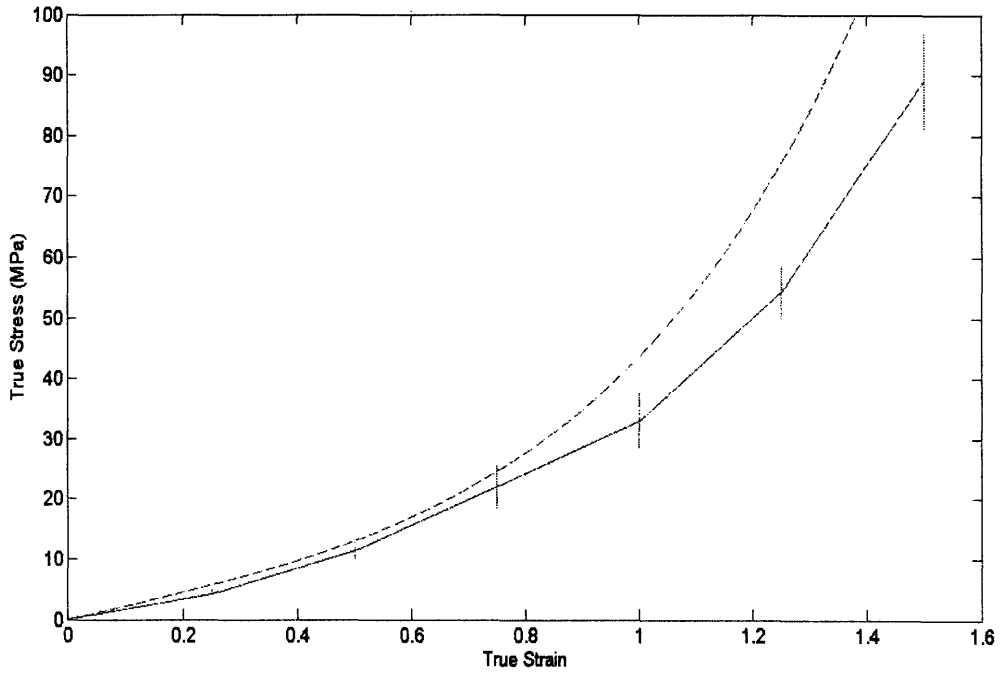

Figure 3.9: True stress vs. true strain for proximal byssal threads. The model is depicted as a dashed line, while the data is depicted as a full line. Note that this full line is an average value curve from all tests. The vertical error bars correspond to an error of one standard deviation from the mean. This plot corresponds to loading at a nominal strain rate of 0.1/s.

Here again, the model predicts the behavior of the thread quite well at lower strains. However, after the yield, the model overpredicts the stress value at a given strain relative to the expected behavior. The behavior is more marked here, since the error bars demonstrate that the model's prediction is outside the one standard deviation range at high strains.

Together these figures demonstrate that the model cannot fully capture the yield behavior of the material. The model predicts a stiffer behavior post-unfolding, whereas the material is in fact much more compliant. Most likely the reason for this is the inability to accurately determine the number density of filament bundles in the thread. Remember that the number of filament bundles in the thread were determined using Figure 1.5, and the method used was simply counting visually and extrapolating from this small thread section to the entire thread. Variance as high as one or two orders of magnitude would not be unlikely; and indeed varying this number density by one or two orders of magnitude did yield different results. However, the value in Table 3.1 was used to determine other important parameters, so it was retained in this model.

Next, the rate-dependence of the model was investigated, by conducting simulations at two different nominal strain rates (0.01/s and 1/s). The nominal stress-nominal strain plot (Figure 3.10) and true stress-true strain plot (Figure 3.11) demonstrate that the model did indeed capture the material's rate-dependence.

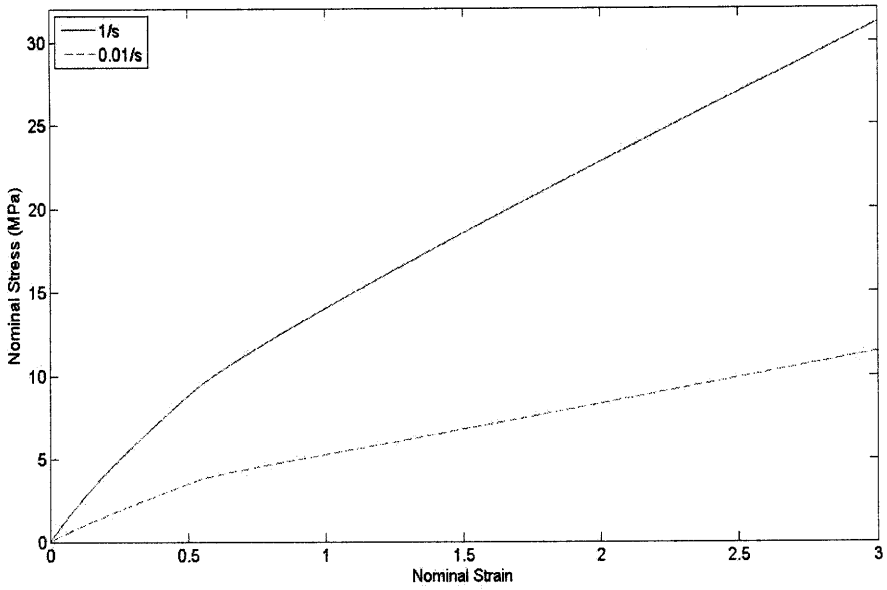

Figure 3.10: Nominal stress vs. nominal strain for proximal byssal threads (computer simulation of loading).

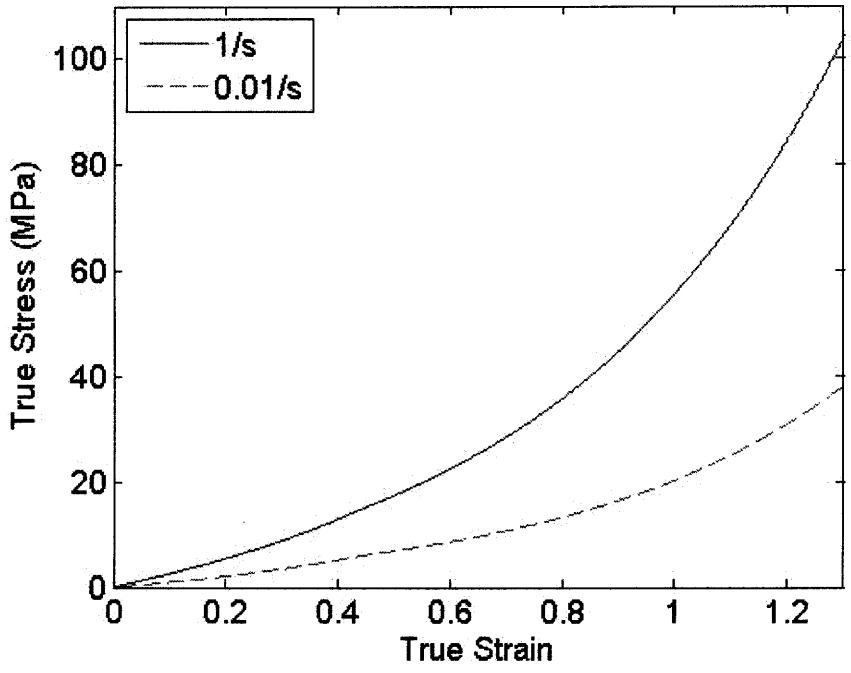

Figure 3.11: True stress vs. true strain for proximal byssal threads (computer simulation of loading).

As a next test for the model, a simulation was conducted for a cyclic testing condition i.e. loading, unloading, and reloading of the thread. The nominal stress vs. nominal strain and true stress vs. true strain results from the simulation are shown in Figure 3.12 and Figure 3.13 respectively.

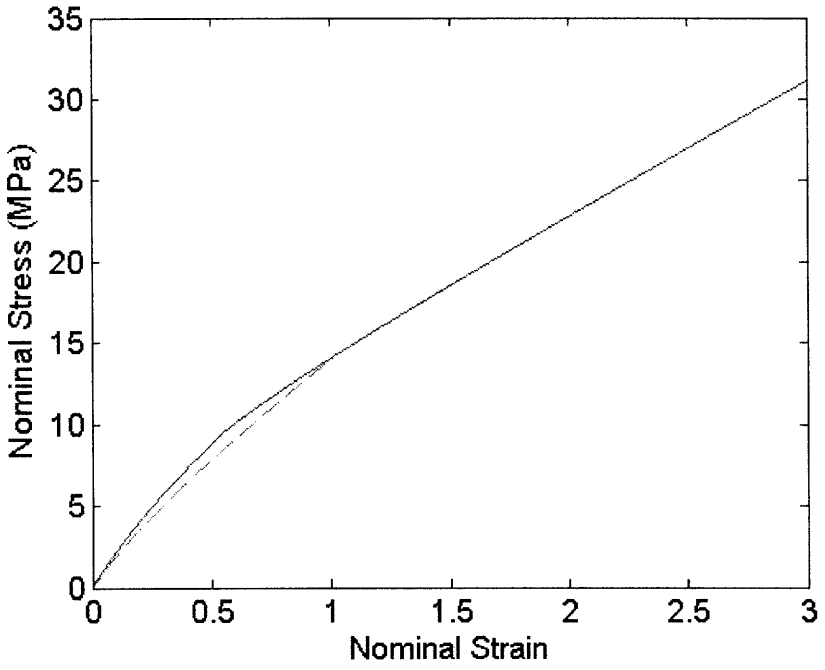

Figure 3.12: Nominal stress vs. nominal strain for computer simulation of proximal byssal thread in loading, unloading, and reloading at a nominal strain rate of 1/s. The dashed line is the unloading line, while the full line is the loading line.

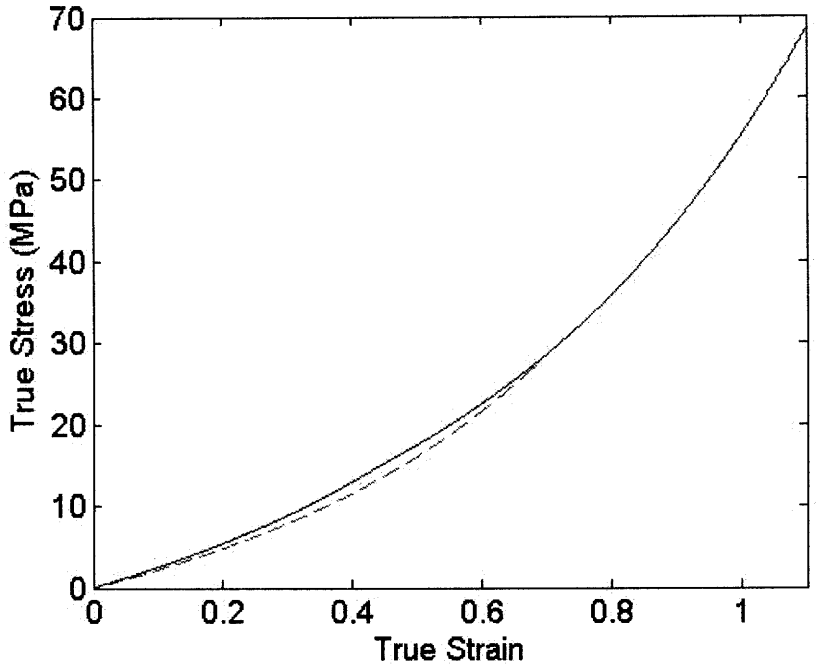

Figure 3.13: True stress vs. true strain for computer simulation of proximal byssal thread in loading, unloading, and reloading at a nominal strain rate of 1/s. The dashed line is the unloading line, while the full line is the loading line.

As can be seen here, the model does demonstrate that the unloading and reloading behavior should be different from the initial loading behavior. However, the unloading curves are much more similar to the initial loading curve than is seen in actual experiments. Further, both the true stress and nominal stress return to zero upon unloading, which is not seen in any of the curves from actual tests. This is more apparent when the data is overlaid, as in Figures 3.14 and 3.15.

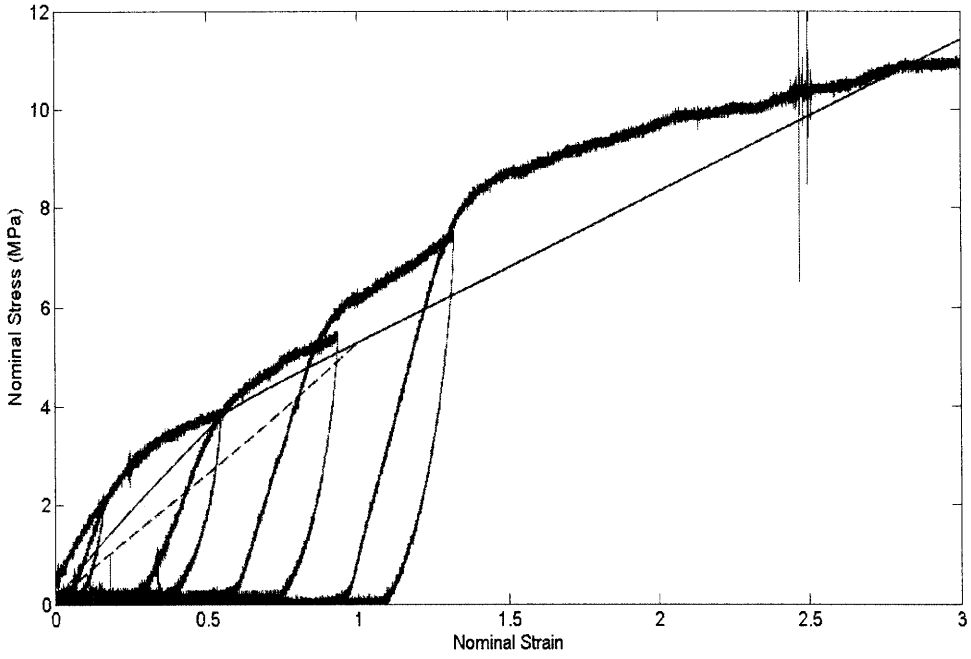

Figure 3.14: Nominal stress vs. nominal strain for proximal byssal threads at a nominal strain rate of 0.01/s. As can be seen, the model (straight full line) captures the initial loading and yield fairly well, but the reloading (dashed line) does not follow the unloading behavior seen in the actual test.

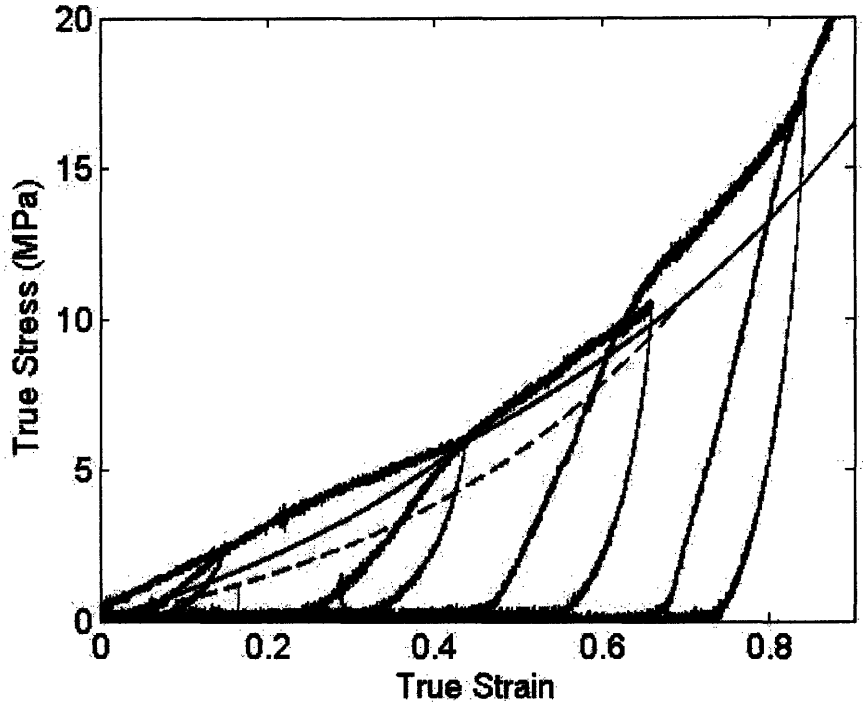

Figure 3.15: True stress vs. true strain for proximal byssal threads at a nominal strain rate of 0.01/s. Again, the overall loading is captured by the model (full line), but the unloading behavior of the model (dashed line) is quite different than that seen in the actual experimental results.

Overall, the proximal model does capture several aspects of the material behavior e.g. the rate-dependence, the "yield" behavior, and the overall shape of the nominal stress-strain and true stress-strain curves. However, it fails to capture the full compliance of the material post-yield and fails to capture the behavior seen in cyclic loading.

As stated above, the exact number density of filament bundles would help to elucidate some of the problems in the model. Further microscopic imaging via transmission electron microscopy would certainly prove beneficial in helping to determine this parameter. On another note, it was assumed in this analysis that the unfolding of each separate bundle was independent of other nearby bundles. If the bundle density is high enough, then it is possible that the unfolding experienced by one bundle would affect the unfolding of other bundles, especially in the proximal section where the bundles are randomly oriented and some "criss-cross" and intertwine.

3.3.2 Distal Section

The distal section was investigated in a manner similar to the proximal section. First, simulations for loading of the distal thread sections to failure were conducted. Figures 3.16 and 3.17 demonstrate the model's ability to predict the nominal stress-nominal strain behavior and true stress-true strain behavior of the distal byssal threads respectively.

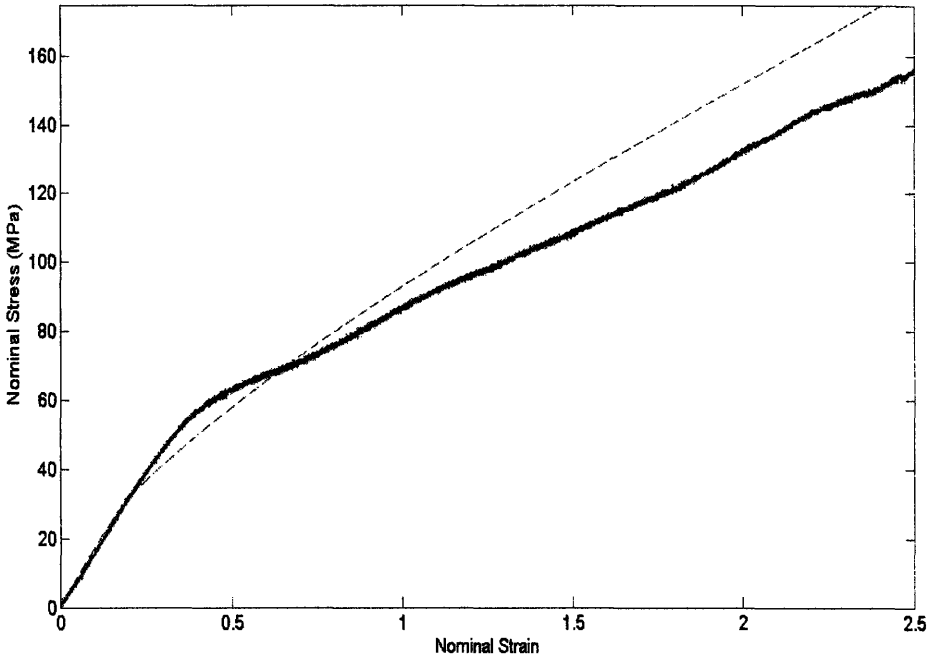

Figure 3.16: Nominal stress vs. nominal strain for distal byssal thread to failure at a nominal strain rate of 0.1/s. The model's prediction is depicted as a dashed line, while the actual experimental data is depicted as a full line.

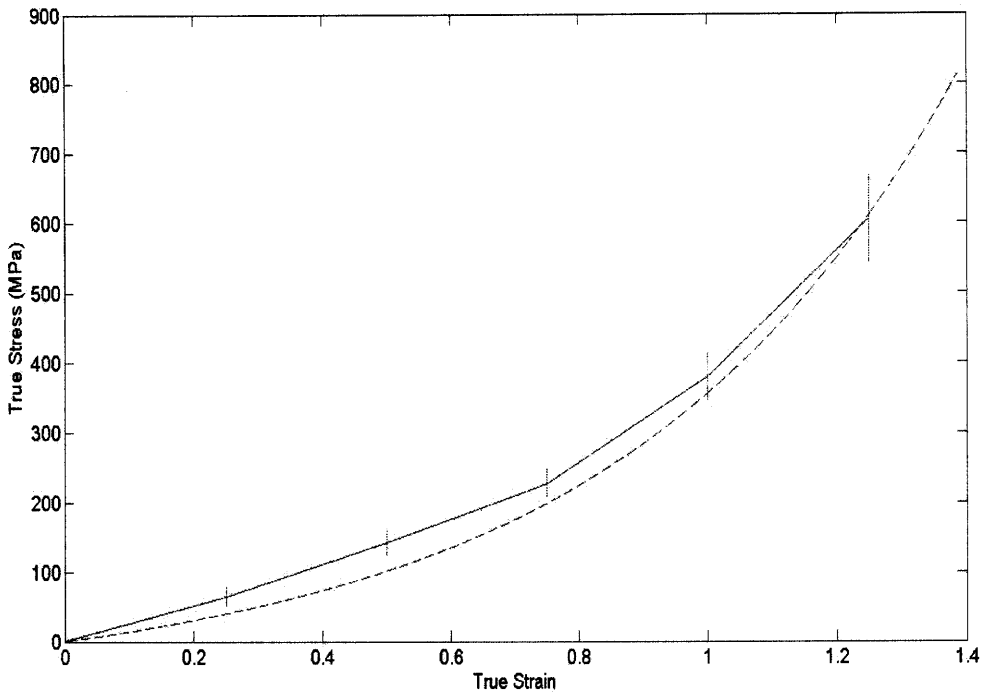

Figure 3.17: Experimental results versus model for distal threads at a strain rate of 0.1/s. Again, the model is given in dashed lines, and the experimental is given with a full line. An average value curve with error bars is employed. Note that here the model predicts a stress below the experimental, but in Figure 3.16 it predicts a stress above the experimental. This is because in Figure 3.16 a characteristic curve is chosen, whereas here an average value curve is used.

For this thread section, the model predicts the experimental data better than for the proximal thread section. However, similar problems exist. For the nominal stress-nominal strain curve, the model captures the initial loading quite well. Further, the model demonstrates a relatively sharp yield as is apparent in the experimental curve. However, just like in the proximal model, the model does not fully predict the post yield compliance of the material, demonstrating a higher slope of the curve post yield.

In spite of these deficiencies, the model is far closer to falling within the one standard deviation error interval of the average value curve, as can be seen in the true stress-true strain data. The shapes of the model curve and the actual experimental curve are also much more similar in the true stress-true strain data (note that the yield is far less apparent in the true stress-true strain curve as discussed above).

The rate-dependence of the material was also investigated, and the model was found to predict the rate-dependence of the material quite well.

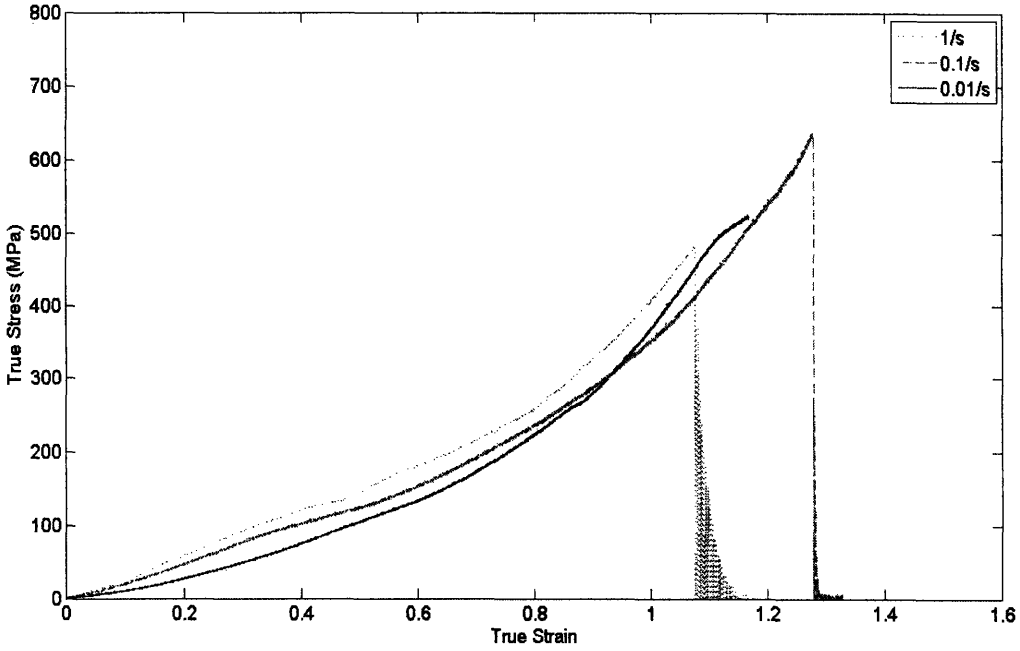

Figure 3.18: True stress vs. true strain for distal threads at three nominal strain rates. Characteristic curves are chosen.

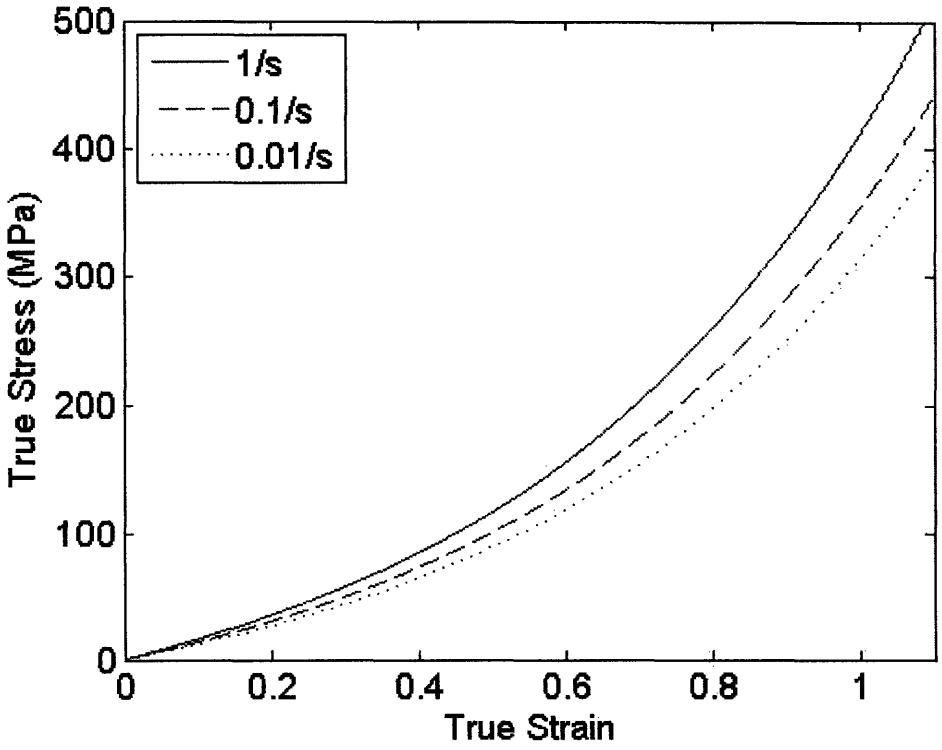

Figure 3.19: Model of the distal thread behavior at the strain rates seen in Figure 3.18

Since the true stress-true strain curves at these three strain rates are so close together, it is hard to fully appreciate the model's ability to predict the rate-dependence. It is easier to comprehend this when looking at nominal stress-nominal strain curves.

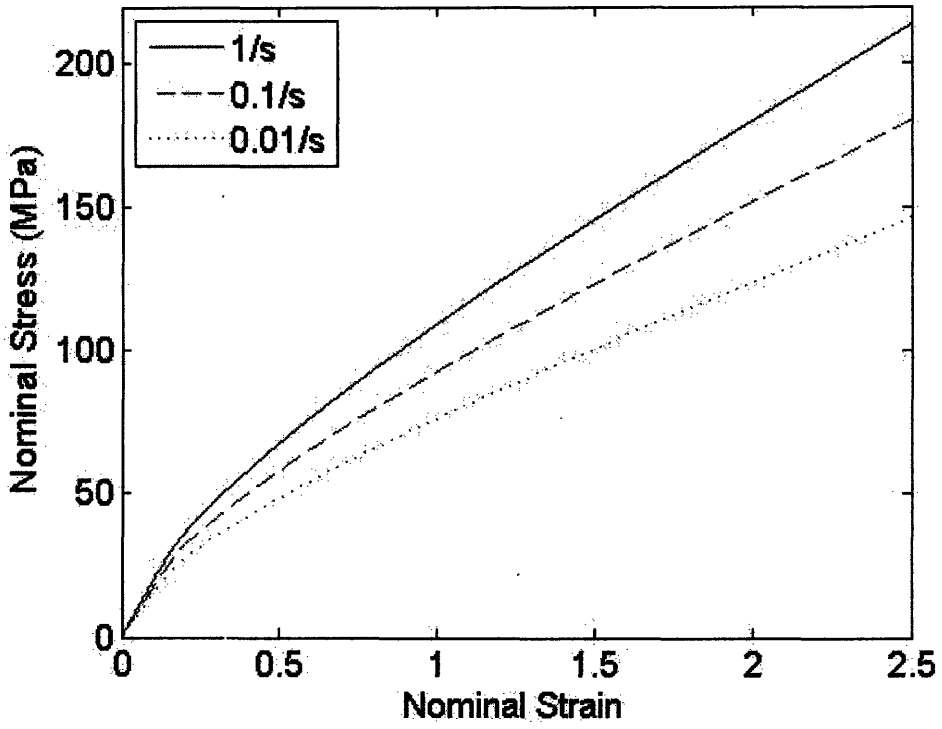

Figure 3.20: Nominal stress vs. nominal strain for distal thread section at varying nominal strain rates (same rates as Figures 3.18 and 3.19).

As can be seen here, the model does indeed demonstrate highly different behavior at the three rates shown. To test whether these values aptly characterize the material behavior, each curve (in true stress-true strain form) was plotted against an average value curve with error bars corresponding to one standard deviation, as was done in the proximal section above.

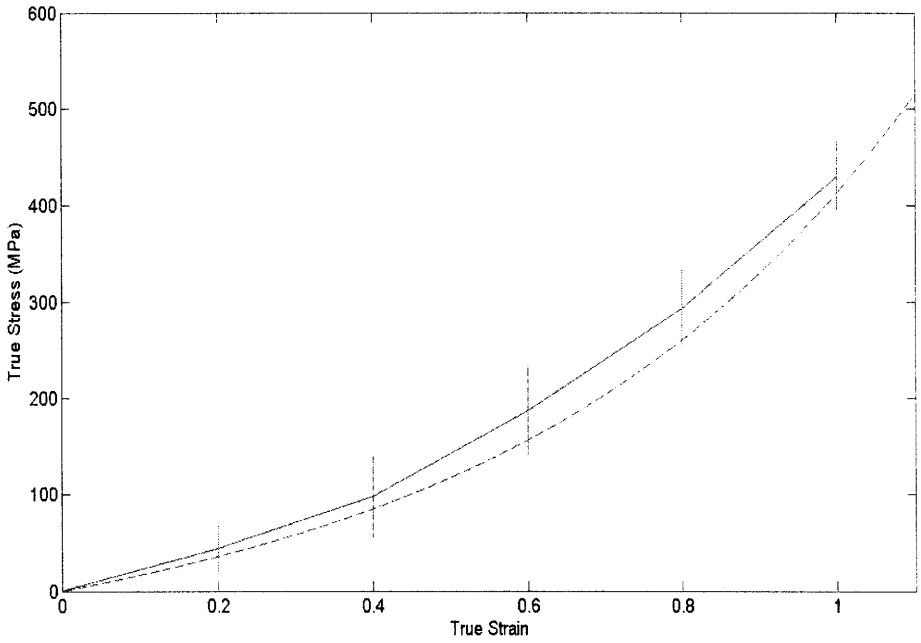

Figure 3.21: Model vs. experimental data for distal thread sections at a strain rate of 1/s. The model is given as a dashed line, whereas the experimental is given as a full line. The experimental curve given here is an average value curve. Error bars correspond to an interval of one standard deviation.

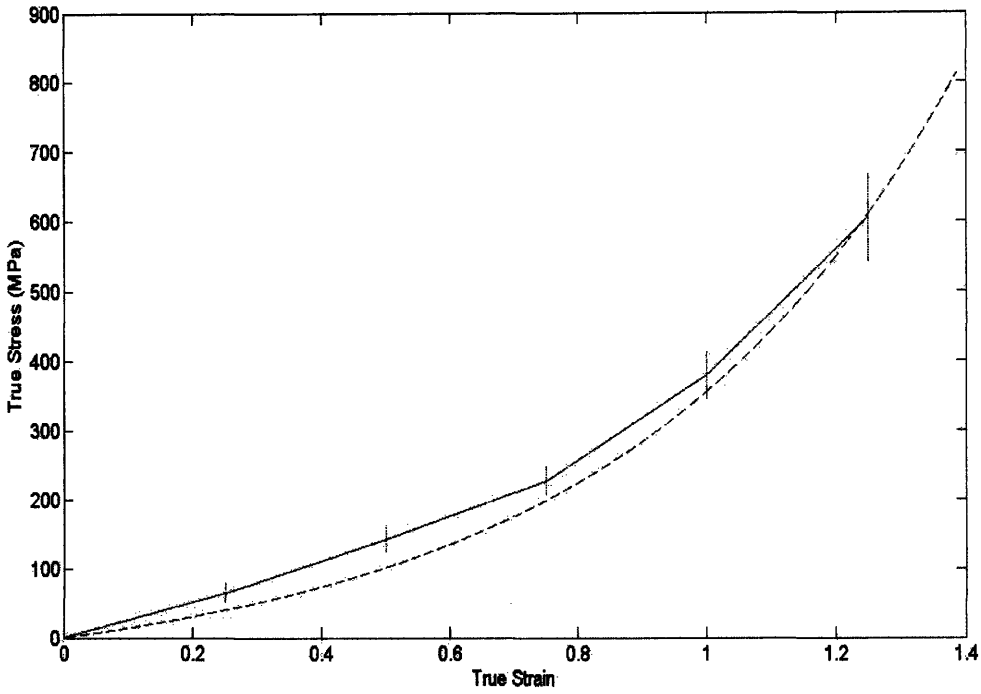

Figure 3.22: Experimental results versus model for distal threads at a strain rate of 0.1/s. Again, the model is given in dashed lines, and the experimental is given with a full line. An average value curve with error bars is employed.

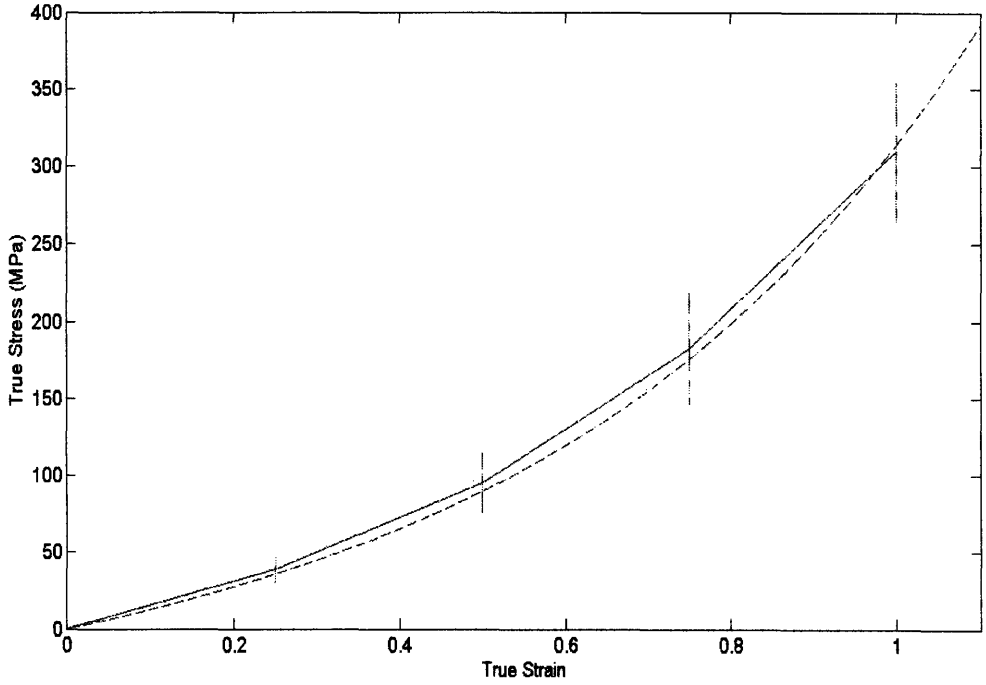

Figure 3.23: Experimental results versus model for distal threads at a strain rate of 0.01/s. Again, the model is given in dashed lines, and the experimental is given with a full line. An average value curve with error bars is employed

As the images depict, for the curves at a nominal strain rate of 0.01/s and 1/s, the model's prediction falls within the one standard deviation error interval at all values of strain. In the case of the strain rate of 0.1/s, the model does deviate from the appropriate error interval at some values of strain, but overall predicts the material behavior quite nicely.

In the case of the test at a strain rate of 0.1/s the model does not deviate from the curve much more than in either of the other two cases, but the error interval is smaller. This is because the tests at 0.1/s were remarkably consistent, with each thread demonstrating a very marked yield (all of which occurred at very nearly the same strain). In the other rate tests, the yields often occurred at markedly different strains. Theoretically there is no reason why some rates should demonstrate repeatable results, while others do not. It is simply one of the pitfalls of studying biological materials. Overall, the model does quite a nice job of predicting the material's rate-dependence.

Finally, the model's ability to predict the material's behavior in cyclic loading was investigated. The results are demonstrated in Figure 3.24 (nominal stress-nominal strain) and Figure 3.25 (true stress-true strain).

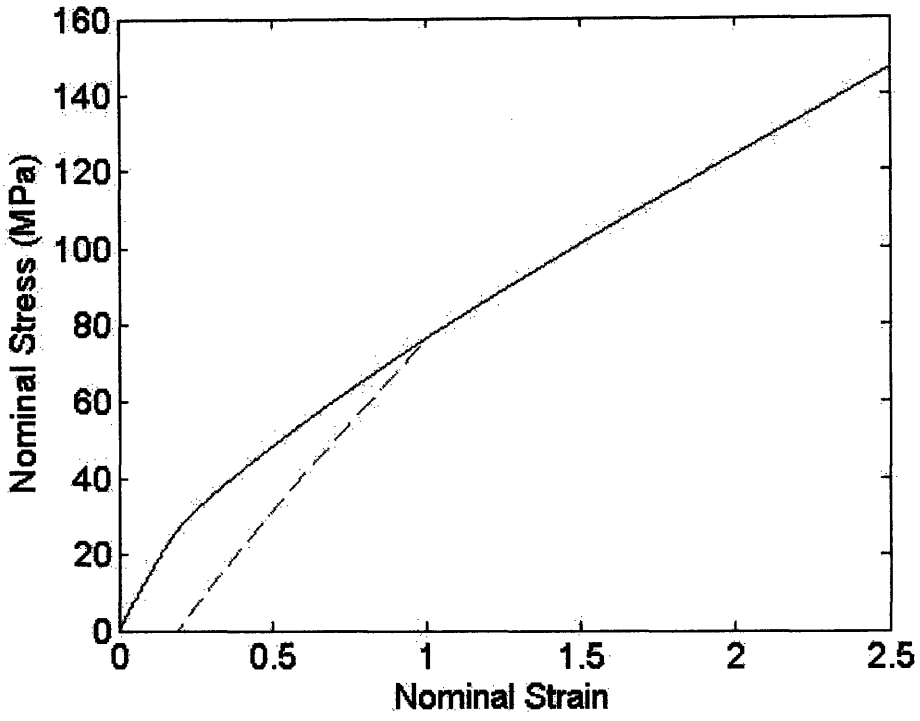

Figure 3.24: Nominal stress vs. nominal strain for loading, unloading, reloading of distal threads at a nominal strain rate of 0.01/s.

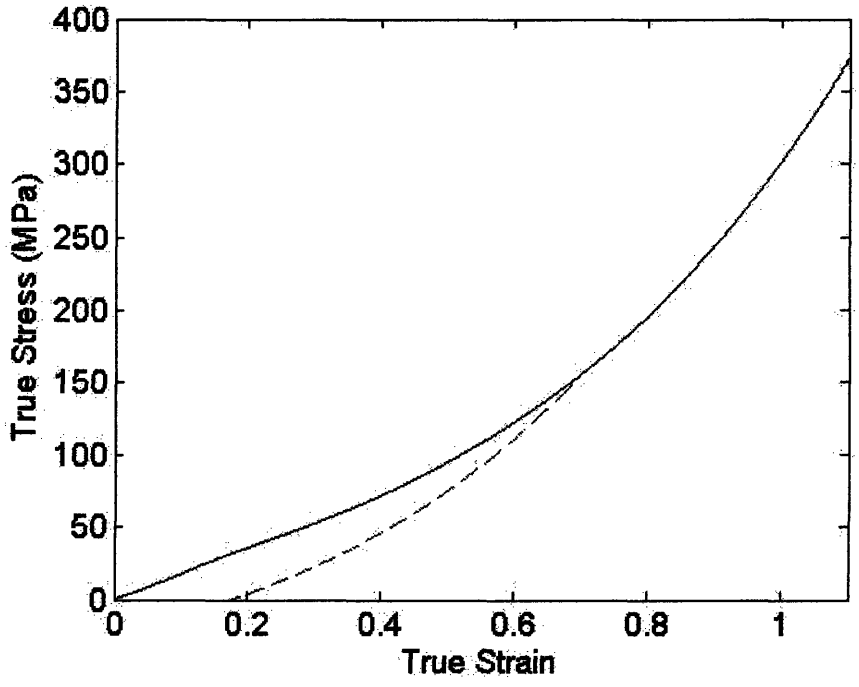

Figure 3.25: True stress vs. true strain for loading, unloading, reloading of distal threads at a nominal strain rate of 0.01/s.

Again the unloading appears to demonstrate a more gradual stress reduction with strain than does the actual material. However, it is far less noticeable than in the proximal model.

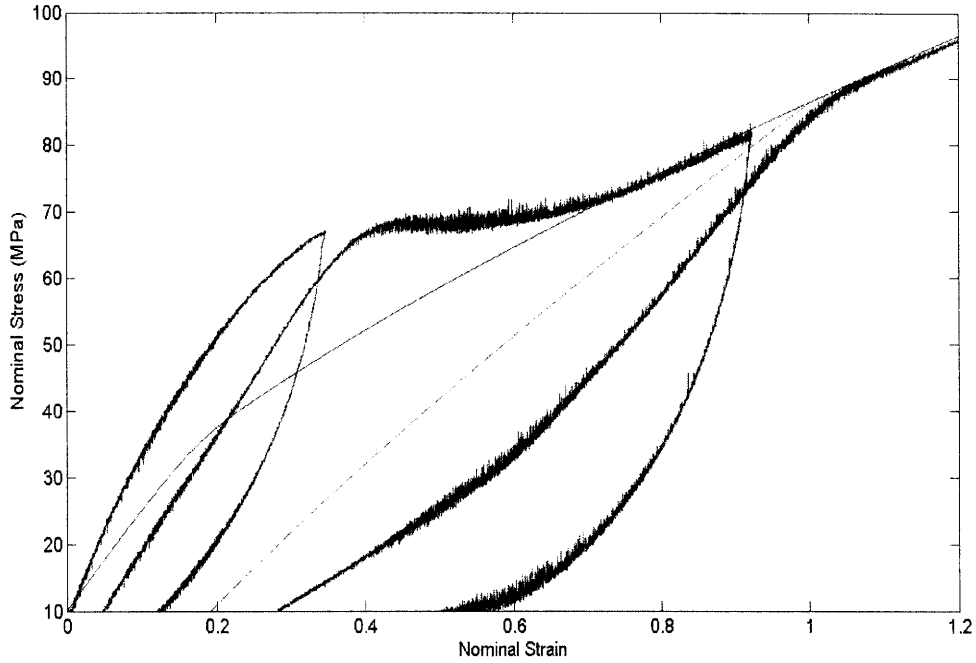

Figure 3.26: Nominal stress vs. nominal strain for model and experimental results for the distal thread section in loading, unloading, and reloading (nominal strain rate of 0.1/s). Note that the full line corresponds to the loading and reloading. The dashed line corresponds to unloading.

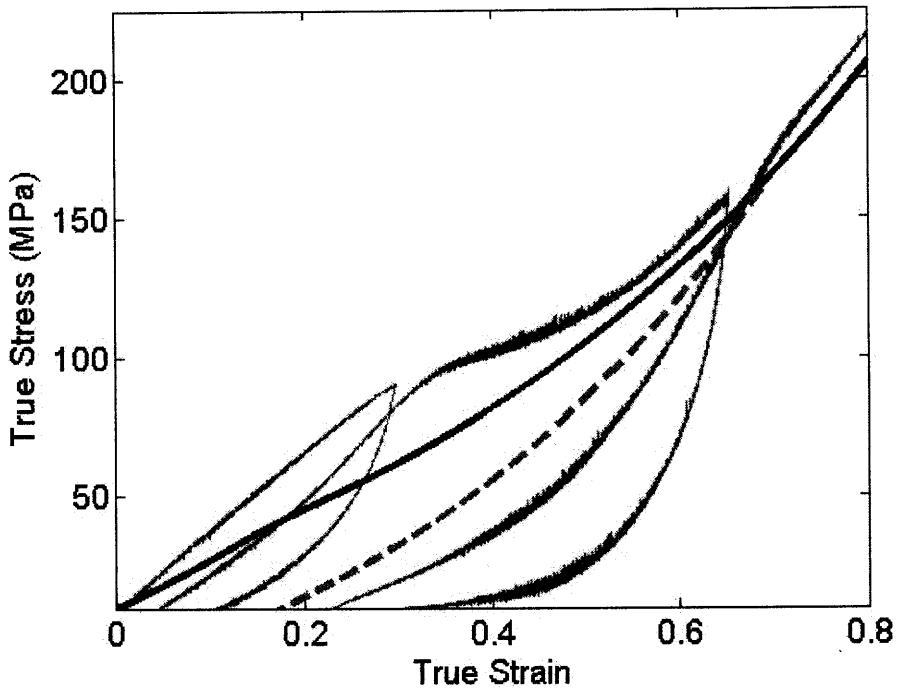

Figure 3.27: True stress vs. true strain for experimental and model results for the distal thread section in loading, unloading, and reloading (nominal strain rate of 0.1/s). Note that the full line corresponds to the loading and reloading. The dashed line corresponds to unloading.

As can be seen the model does not predict the unloading behavior of the material very well. Rather, it predicts that the material will drop in stress more gradually with strain than is seen.

The reasons for this discrepancy are similar to that in the proximal thread section. Though, the alignment of the bundles does not come into play, as they are known to be aligned. This also implies that the affects of one bundle on another are minimal.

3.4 Possible Reasons for Model Deficiencies

Many material properties were taken from previous literature including the geometry of the fiber bundles with respect to diameter, initial length, and maximum length. Varying these parameters was found to heavily affect the model's prediction. Most importantly the density of the filament bundles within the threads was estimated from previously existing images. Imaging of an entire thread would be helpful in determining this parameter more accurately. Finally, the modulus of the jelly matrix (related to C in the above equations) proved to be important throughout conducting the simulations.

The deficiencies of the model to predict the unloading behavior of the model seems to be the most heavily dependent on these factors. It is most likely that the bundles would not heavily affect neighboring bundles in the distal section, since the bundles are aligned with the thread axis. However, in the proximal section, it would seem that this could be a

concern. In the actual simulations, it was demonstrated that the model predicted the behavior better in the distal section than in the proximal (as is expected if this interplay is important). Investigation of bundle affects on neighbors, and introduction of such a factor into modeling, would surely provide a better overall material model.

Chapter Four: Conclusions

The mechanical behavior of mussel byssal threads was here investigated. An array of tests (monotonic and cyclic) at varying nominal strain rates was conducted on both thread sections – proximal and distal. The proximal thread demonstrated an initially stiff modulus, with a continuous and gradual rollover type "yield" phenomenon, followed by a much more compliant behavior. The section was found to be highly extensible, reaching axial stretches greater than four ($\lambda > 4$) prior to failure. The distal section demonstrated an initial modulus that was somewhat stiffer than the proximal. This was followed by a "yield" phenomenon, not unlike the proximal threads. However, for the distal threads, the "yield" was far more sudden, transitioning the material quite suddenly into a regime of much more compliance. The distal thread was also found to be quite extensible, though less so than the proximal, reaching axial stretches of approximately 2.5 prior to failure ($\lambda \approx 2.5$).

A model was developed to predict the response of this material to loading in uniaxial tension; a separate model was formulated for each of the two thread sections. The models were based mainly on the evolution of the microstructure of each thread section. This microstructure consisted of filament bundles with folded domain ends, which unfolded upon loading. The models were shown to partially predict the behavior of the material in monotonic and cyclic loading. The "yield" phenomenon was captured for each thread section, as well as the rate-dependence. The difference in material behavior during loading and unloading was also captured. In spite of these strengths, the model was deficient in a few areas. First, the model did not fully capture the compliance of the material post-yield (for both thread sections). Similarly, the model did not capture the exact nature of the reloading for the cyclic tests. Finally, the model could not consistently predict the exact value of strain at which yield occurred.

The overall equations used in the model seem to capture the behavior of the material quite well, especially the Eyring Model used for the unfolding of the filament bundles. Thus, the model's deficiencies are most likely a result of incorrect parameters rather than poor equations. As discussed above, many parameters are interdependent e.g. n, A, and E, and varying one parameter affects the accuracy and efficacy of the other parameters. Also, several parameters were taken from previous literature, such as L_{max} and variance in these parameters also significantly affects the model. Finally, no parameter was introduced for refolding of filament bundles during unloading. This should prove to be quite important in the model's ability to predict the material behavior in cyclic loading.

Future work on this model should prove extremely useful. Tests at more strain rates would help in determining more exact values for several of the parameters. Further, relaxation tests would prove useful in determining whether refolding can be captured by changing existing equations or introducing new equations. Finally, microscopic imaging e.g. TEM or SEM imaging would prove extremely useful in determining the exact microscopic makeup of the threads especially with respect to the alignment of filament bundles and their number density within the thread.

Acknowledgements

The research in this thesis would not have been possible without guidance and assistance from Professor Mary C. Boyce, Dr. Katia Bertoldi, and Meredith Silberstein. I appreciate the time and dedication they put into making this project possible, Meredith in particular for training in most aspects of the experimental portion of the thesis, and Katia for all her help with modeling.

References

[1] Alper, J., 2002. Stretching the Limits. Science. 297, 329-330.

[2] Bairati, A.,1991. The byssus of the mussel Mytilus from the molecules to the organ: functional performance resides in the ultrastructural assembly. In Form and function in zoology (ed. G. Lanzavecchia and R. Valvassori), pp. 163-177. Modena: Mucchi.

[3] Bairati, A., Vitellaro-Zuccarello, L., 1974. The ultrastructure of the byssal apparatus of Mytilus galloprovincialis. III. Analysis of byssus characteristics by polarized light microscopy. Journal of Submicroscopic Cytology. 6, 367-379

[4] Bairati, A., Vitellaro-Zuccarello, L., 1976. The ultrastructure of the byssal apparatus of Mytilus galloprovincialis. IV. Observations by transmission electron microscopy. Cell Tiss. Res. 166, 219-234.

[5] Bell, E., Gosline, J.M., 1996. Mechanical design of mussel byssus: material yield enhances attachment strength. The Journal of Experimental Biology 199, 1005-1017.

[6] Benedict, C.V., Waite, J.H., 1986. Composition and ultrastructure of the byssus of mytilus edulis. Journal of morphology 189, 261-270.

[7] Bertoldi, K., and Boyce, M.C., 2007, Mechanics of the hysteretic large strain behavior of mussel byssal threads, Journal of Materials Science, 42, 8943-8956.

[8] Carrington, E., Gosline, J.M., 2004. Mechanical design of mussel byssus: load cycle and strain rate dependence. American Malacological Bulletin, 18, 135-142.

[9] Coyne, K.J., Qin, X.X., Waite, J.H., 1997. Extensible collagen in mussel byssus: a natural block copolymer. Science 277, 1830-1832.

[10] Eckroat, L.R., Steele, L.M., 1993. Comparative morphology of the byssi of Dreissena Polymorpha and Mytilus Edulis. American Malacological Bulletin. 10(1), 103-108.

[11] Gosline, J.M., Guerette, P.A., Ortlepp, C.S., Savage, K.N., 1999. The mechanical design of spider silks: from fibroin sequence to mechanical function. J. Exp. Biol. 202, 3295-3303.

[12] Hassenkam, T., Gutsmann, T., Hansma, P., Sagert, J., Waite, J.H., 2004. Giant bent-core mesogens in the thread forming process of marine mussels. Biomacromolecules 5, 1351-1355.

[13] Rief, M., Gautel, M., Oesterhelt, F., Fernandez, J.M., Gaub, H.E., 1997. Reversible unfolding of individual titin immunoglobulin domains by AFM. Science. 276, 1109.

[14] Silverman, H.G., Roberto, F.F., 2007. Understanding marine mussel adhesion. Marine Biotechnology Review. 9, 661-681.

[15] Sun, C., Vaccaro, E., Waite, J.H., Oxidative stress and the mechanical properties of naturally occurring chimeric collagen-containing fibers. 2001. Biophysical Journal. 81, 3590-3595.

[16] Sun, C., Waite, J.H., 2005. Mapping chemical gradients within and along a fibrous structural tissue, mussel byssal threads. Journal of Biological Chemistry. 280, 39332-39336.

[17] Waite, J.H., Qin, X.X., Coyne, K.J., 1998. The peculiar collagens of mussel byssus. Matrix biology 17, 93-108.

Appendix: Results for All Tests

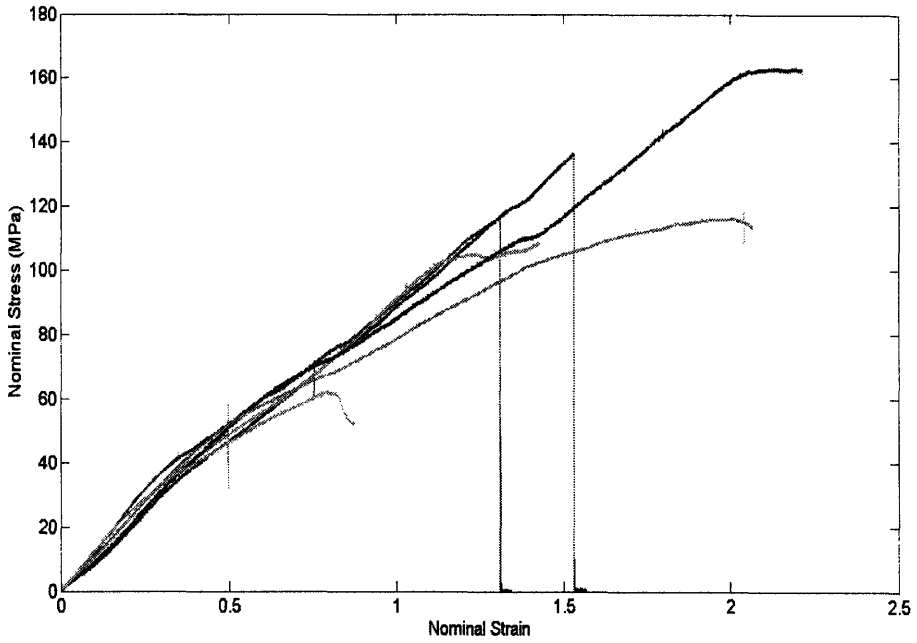

Figure A.1: Nominal stress vs. nominal strain for distal byssal threads at a strain rate of 0.01/s.

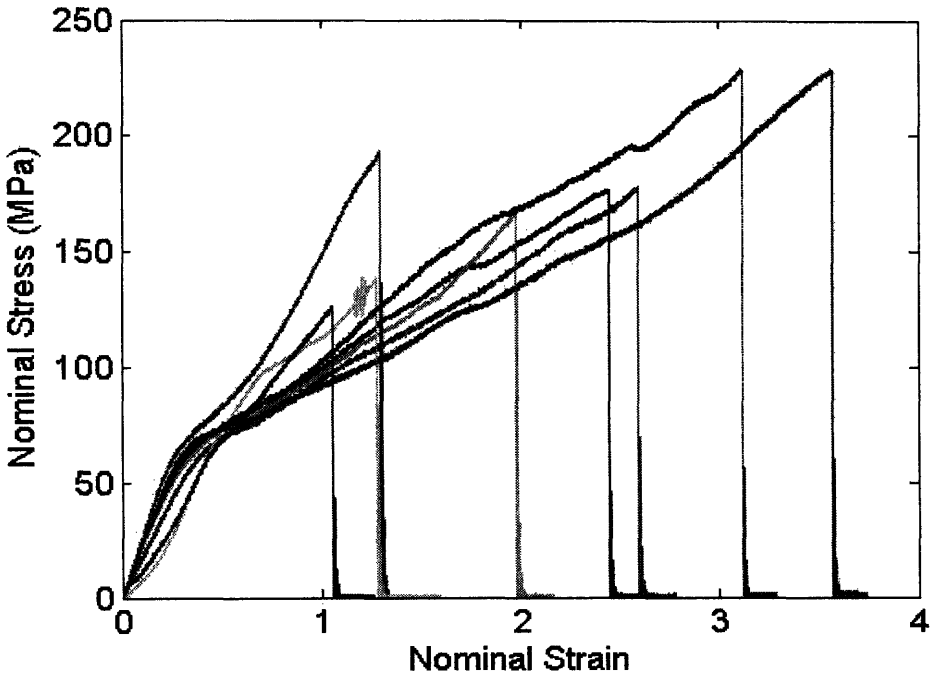

Figure A.2: Nominal stress vs. nominal strain for distal byssal threads at a strain rate of 0.1/s.

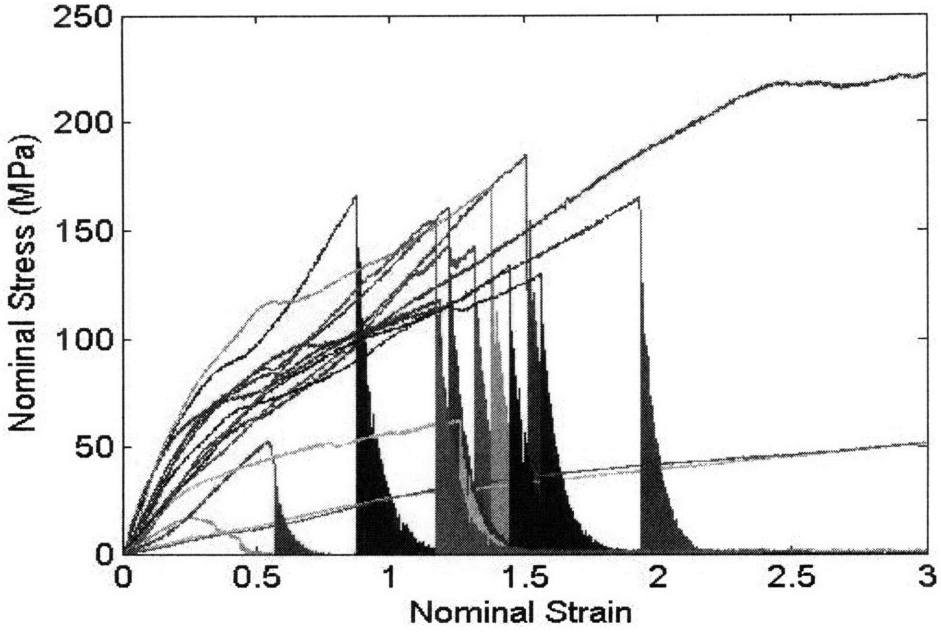

Figure A.3: Nominal stress vs. nominal strain for distal byssal threads at a strain rate of 1/s.

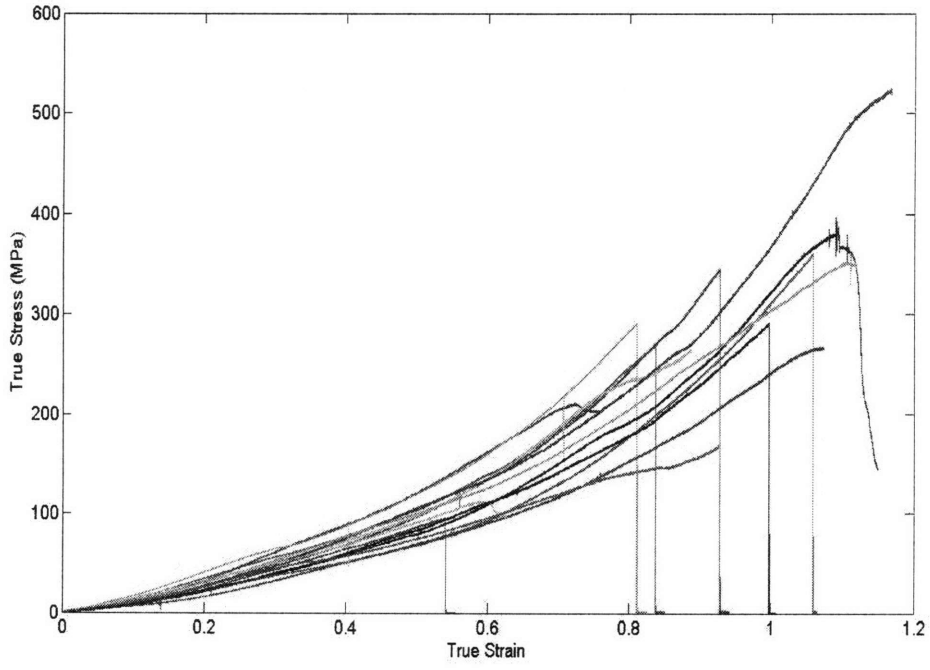

Figure A.4: True stress vs. true strain for distal byssal threads at a strain rate of 0.01/s.

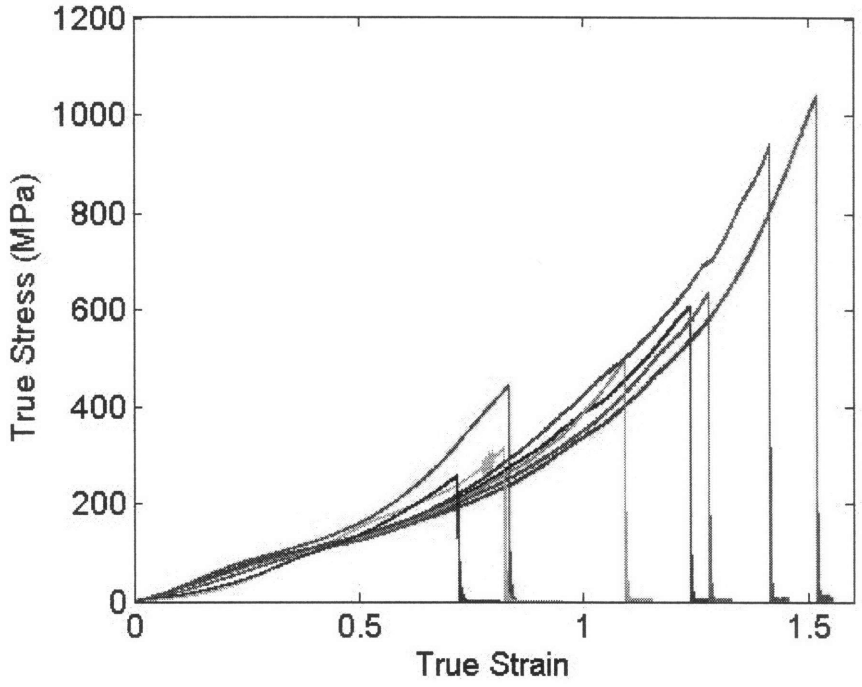

Figure A.5: True stress vs. true strain for distal byssal threads at a strain rate of 0.1/s.

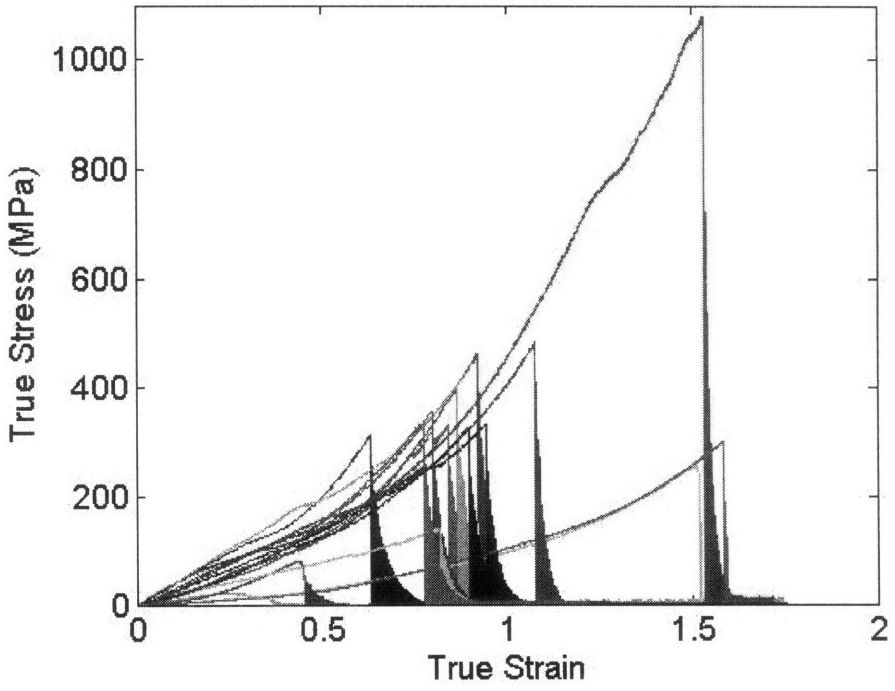

Figure A.6: True stress vs. true strain for distal byssal threads at a strain rate of 1/s.

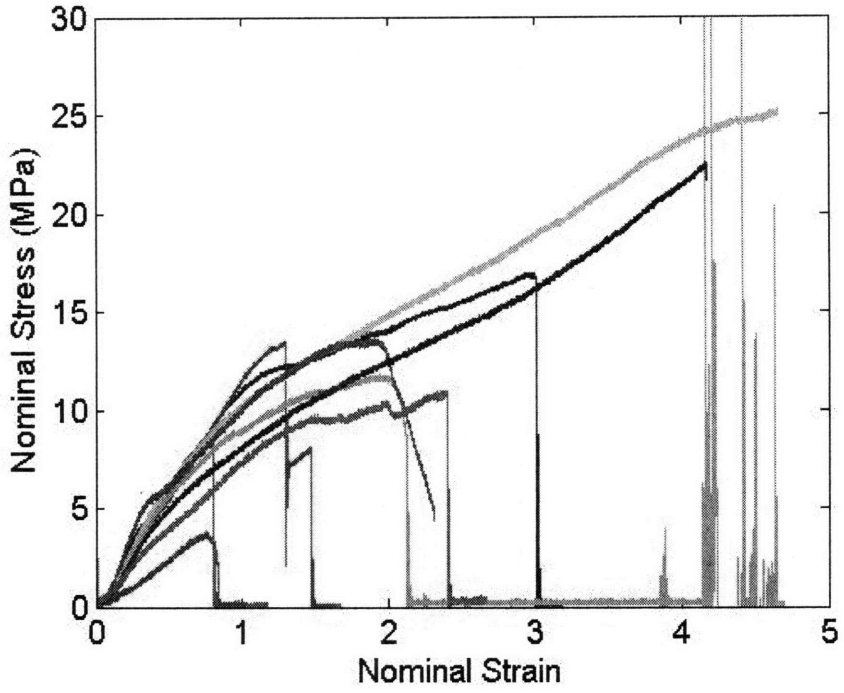

Figure A.7: Nominal stress vs. nominal strain for proximal byssal threads at a strain rate of 0.1/s.

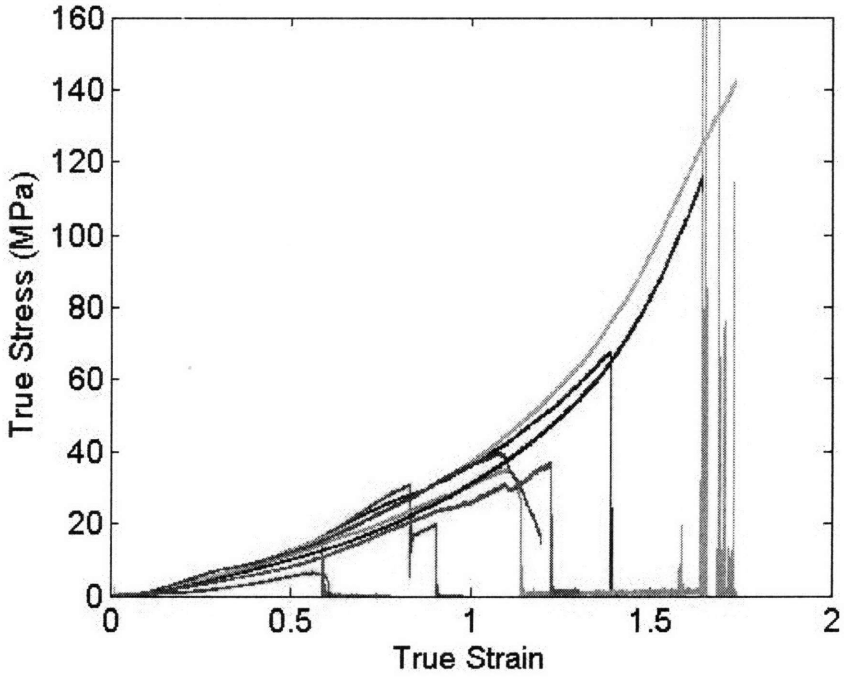

Figure A.8: True stress vs. true strain for proximal byssal threads at a strain rate of 0.1/s.

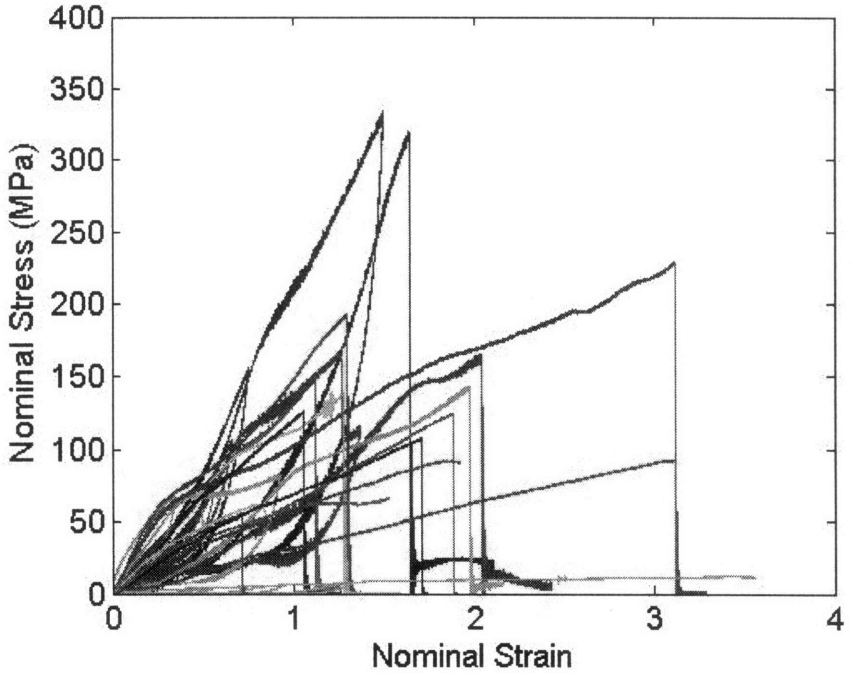

Figure A.9: Nominal stress vs. nominal strain for cyclic tests on distal thread section at a strain rate of 0.1/s.

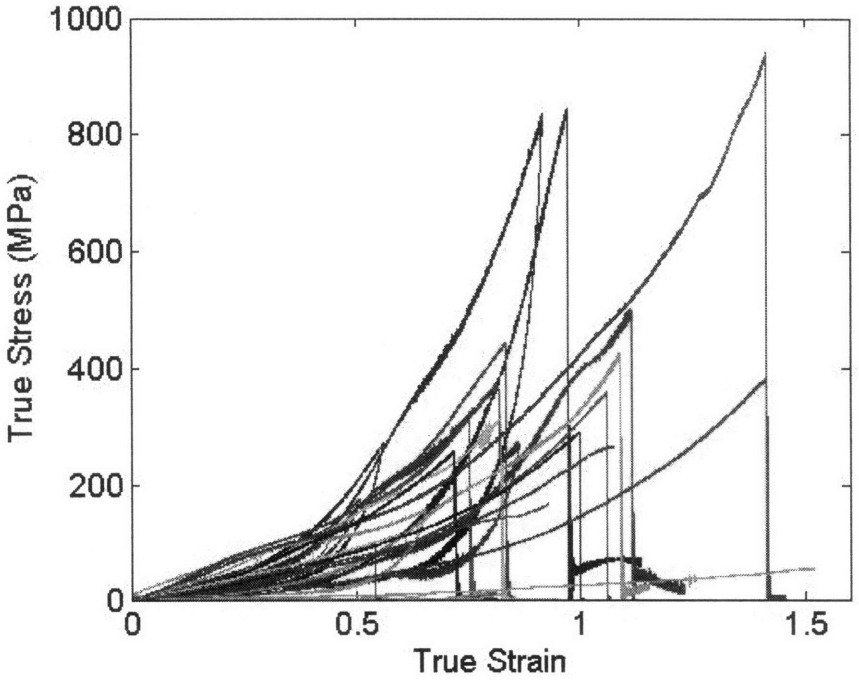

Figure A.10: True stress vs. true strain for cyclic tests on distal thread section at a strain rate of 0.1/s.

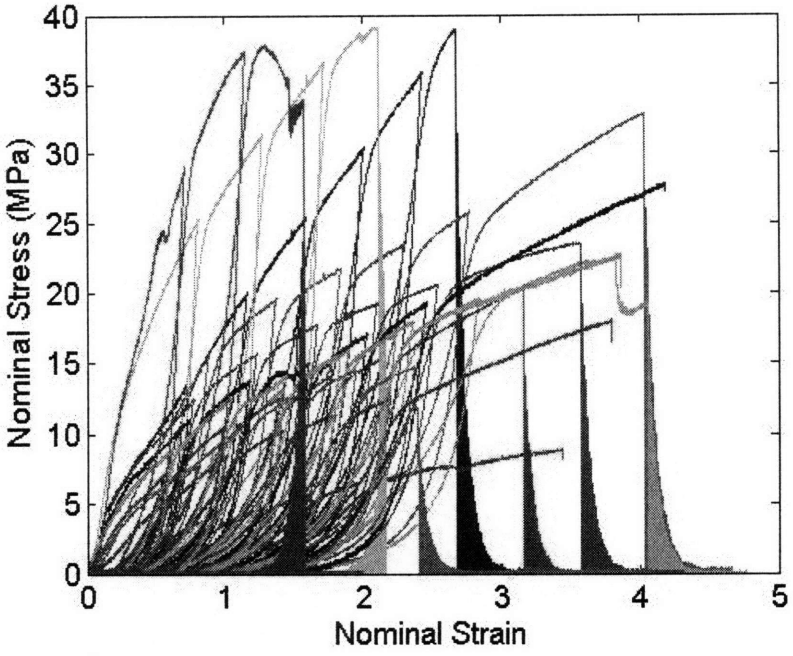

Figure A.11: Nominal stress vs. nominal strain for cyclic tests on proximal thread sections at a strain rate of 1/s.

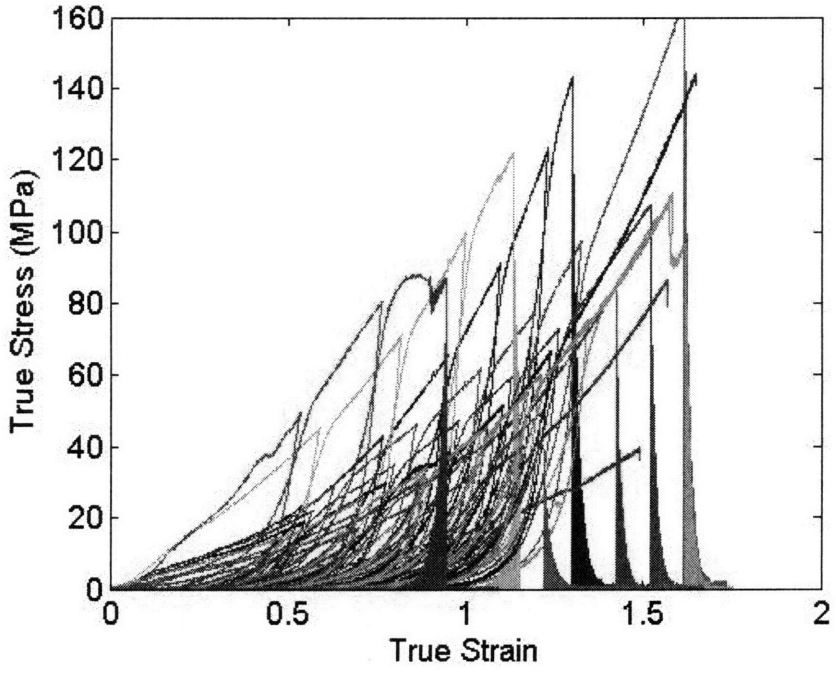

Figure A.12: True stress vs. true strain for cyclic tests on proximal thread sections at a strain rate of 1/s.

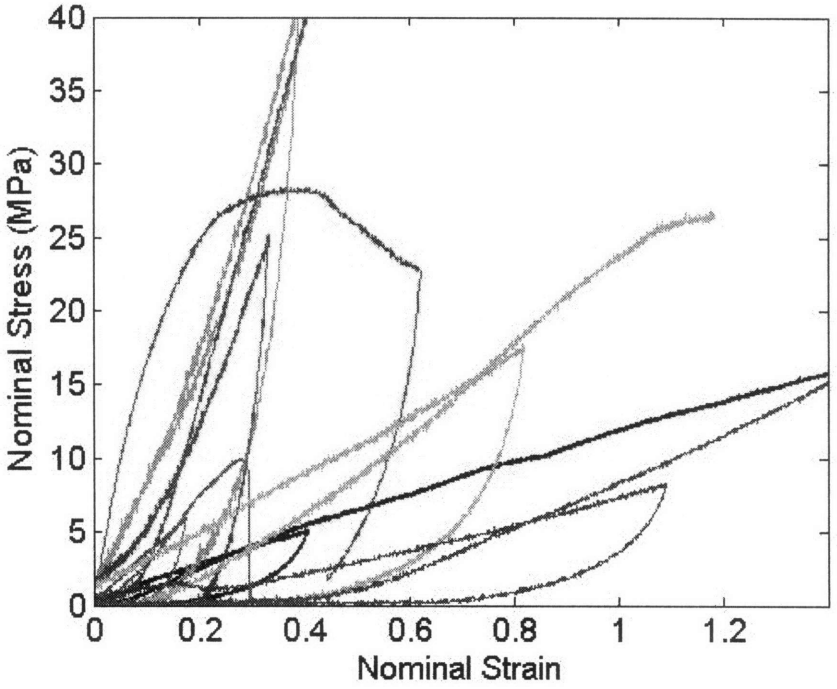

Figure A.13: Nominal stress vs. nominal strain for cyclic tests with a 3 min. hold time between cycles for proximal thread section at a strain rate of 0.1/s.

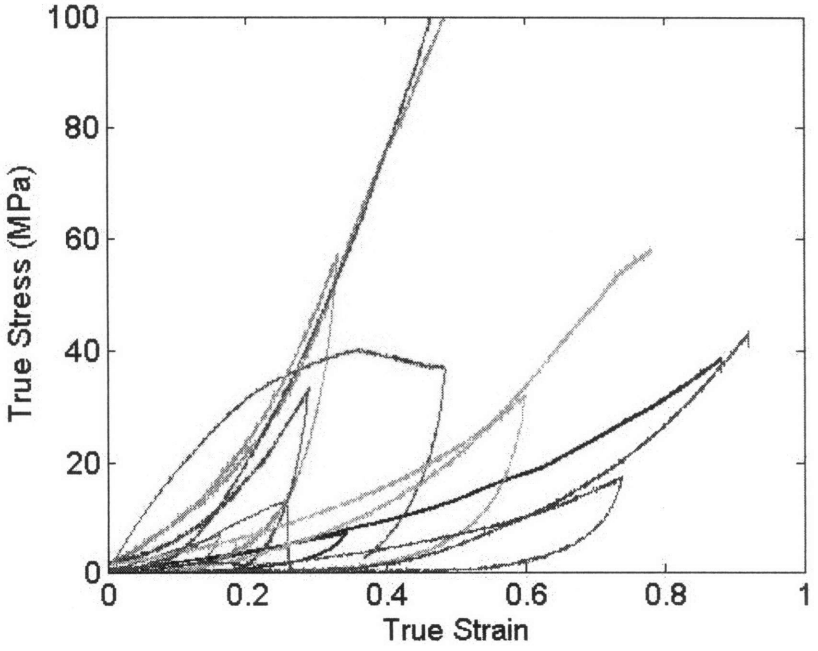

Figure A.14: True stress vs. true strain for cyclic tests with a 3 min. hold time between cycles for proximal thread section at a strain rate of 0.1/s.